## Identification of Optimal Composition with Superior Electrochemical Properties Along the Zero Mn<sup>3+</sup> Line in Na<sub>0.75</sub>(Mn-Al-Ni)O<sub>2</sub> Pseudo Ternary System

Hari Narayanan Vasavan <sup>a</sup>, Manish Badole <sup>a</sup>, Samriddhi Saxena <sup>a</sup>, Velaga Srihari<sup>b</sup>, Asish Kumar Das <sup>a</sup>, Pratiksha Gami <sup>a</sup>, Neha Dagar <sup>a</sup>, Sonia Deswal <sup>c</sup>, Pradeep Kumar <sup>c</sup>, Himanshu Kumar Poswal <sup>b</sup>, and Sunil Kumar <sup>a,d,\*</sup>

<sup>a</sup> Department of Metallurgical Engineering and Materials Science, Indian Institute of Technology Indore, Simrol, 453552, India.

<sup>b</sup> High Pressure & Synchrotron Radiation Physics Division, Bhabha Atomic Research Centre, 400085 Mumbai, India

<sup>c</sup> School of Physical Sciences, Indian Institute of Technology Mandi, Himachal Pradesh, 175005, India

<sup>d</sup> Center for Electric Vehicle and Intelligent Transport Systems, Indian Institute of Technology Indore, Simrol, 453552, India.

\* Corresponding Author: sunil@iiti.ac.in

#### **Abstract**

Biphasic layered oxide cathodes, known for their superior electrochemical performance, are prime candidates for commercializing Na-ion batteries. Herein, we unveil a series of P3/P2 monophasic and biphasic Al-substituted Na $\frac{3}{4}$ Mn $\frac{5-x}{8}$ Al $\frac{2x}{8}$ Ni $\frac{3-x}{8}$ O $_2$  layered oxide cathodes which lie along the 'zero  $Mn^{3+}$  line' in the Na $\frac{3}{4}$ (Mn-Al-Ni)O $_2$  pseudo-ternary system. The structural analysis showed an increased Na $^+$  conduction bottleneck area in both P3 and P2 structures with an increased Al $^{3+}$  content, which enhanced the rate performance of Al-substituted samples. In each composition, the P3/P2 biphasic compound with nearly equal fractions of P3 and P2 phases outperformed their monophasic counterparts in almost all electrochemical performance parameters. Operando Synchrotron XRD measurements obtained for the monophasic P3 and biphasic P2/P3 samples revealed the absence of the O3 phase during cycling. The high structure stability and faster Na $^+$  transport kinetics in the biphasic samples underpins the enhancement of electrochemical properties in the Al-substituted P3/P2 cathodes. These results highlight fixed oxidation state lines as a novel tool to identify and design layered oxide cathodes for Na-ion batteries in pseudo-ternary diagrams involving Jahn-Teller active cations.

**KEYWORDS**: Layered oxides; Biphasic cathode; Operando Synchrotron XRD; Electrochemical behavior; Cyclic performance

#### 1. Introduction

Na-ion batteries (NIBs) offer an alternative to complement or replace the existing Li-ion batteries (LIBs) [1]. With the natural abundance of Na, NIBs transcend the cost limitations posed by LIBs and can contribute to developing sustainable and cost-effective energy storage solutions [2-7]. A major challenge in adopting Na-ion battery technology stems from the low energy density of their cathode materials. Currently, the research into Na-based cathode materials is concentrated on 3 types: NASICON, layered oxides (LOs), and Prussian blue analogs. Among these, layered oxide-based cathodes (due to their compositional diversity and higher energy densities) hold the highest potential for commercialization [6-9]. Layered oxide (LO) compounds (with a general formula  $Na_xTMO_2$ ;  $0 < x \le 1$ ; TM- transition metal cations) exhibit a variety of structures, such as P2, P3, O3, and O2, where the Na ions reside in prismatic (P type phases) and octahedral sites (O type phases) [10]. In terms of electrochemical properties, the P2 type frameworks show higher ionic conductivity and structural stability but suffer from low specific capacities [8, 11-15]. In contrast, O3 type materials exhibit relatively higher specific capacities but are known to undergo O3 to P3 phase transformations during desodiation, limiting their cyclability [16-19]. P3 type compounds, on the other hand, have properties similar to P2 phases. These are known to have good Na<sup>+</sup> transport properties and form at lower calcination temperatures, which makes them easier to synthesize [18, 20-22].

Hence, the introduction of biphasic cathode materials involving different concentrations of O3 and P2 type phases has been widely studied to enhance the electrochemical performance of layered oxide cathodes [23-29]. In O3/P2 biphasic cathodes, the synergistic effect arising from the coexistence of P2 and O3 type phases has been reported to enhance structural stabilities and Na<sup>+</sup> transport kinematics, leading to better rate performance and cyclic performance [25, 30, 31]. Although not as extensively studied, P2/P3 biphasic cathodes also

show similar enhancement in electrochemical properties due to an interlocking of P3 and P2 structures [26, 32-34]. These materials have shown higher rate performance compared to their monophasic counterparts. Combining P3 and P2 type phases also leverages the superior Na<sup>+</sup> transport properties of both phases; the biphasic P3 and P2 type compounds can be obtained at relatively lower calcination temperatures compared to P2 and O3 type phases. Another method commonly used to improve the electrochemical performance in layered oxides is partially incorporating electrochemically inactive ions, such as Mg<sup>2+</sup>, Al<sup>3+</sup>, Zn<sup>2+</sup>, etc., in the transition metal layers [35-40]. As the name suggests, such ions remain electrochemically inactive and act as pillar ions that stabilize the structure during cycling. Although not extensively studied in NIB cathodes, Al<sup>3+</sup> substitution in layered oxides is reported to enhance the rate performance and cyclic stability of LIB cathodes [38, 41-44].

The current study explores the structural and electrochemical properties of P3/P2 biphasic cathodes in the Na<sub>3/4</sub>(Mn-Al-Ni)O<sub>2</sub> system. The compounds, with a general formula Na<sub>3</sub>Mn<sub>5-x</sub>Al<sub>2x</sub>Ni<sub>3-x</sub>O<sub>2</sub> (x = 0, 0.25, 0.50, 0.75, and 1), lie on the so-called 'zero  $Mn^{3+}$  line' (Fig. 1 and S1) in the Na<sub>3/4</sub>(Mn-Al-Ni)O<sub>2</sub> pseudo-ternary phase diagram. Phase diagrams, especially in layered oxides, help to rationally design optimal cathode compositions by revealing the complex relationship between metal cations in LO cathodes and different electrochemical properties [45, 46]. It is important to point out that, unlike a traditional phase diagram, where the elemental compositions alone largely determine the functional properties of various phases, in a pseudo-ternary system, the oxidation states of the electrochemically active elements involved also play a major role in deciding composition-structure-property behavior. Therefore, the 'zero  $Mn^{3+}$  line' identified in this study confines the Mn ions to a 4+ oxidation state by varying the concentration of Mn, Ni, and Al ions. This novel approach differs from the conventional method of analyzing ternary diagrams in which the concentration of at least one of the elements remains constant. Moreover, in the Na<sub>3/4</sub>(Mn-Al-

Ni)O<sub>2</sub> pseudo-ternary system, the 'zero  $Mn^{3+}$  line' is also the boundary between the forbidden region (assuming Ni is only allowed to maintain a 2+ oxidation state) and the allowed region.

Recently, studies have reported the structural and electrochemical properties of monophasic and biphasic Na<sub>0.75</sub>Mn<sub>0.75</sub>Ni<sub>0.25</sub>O<sub>2</sub> and Na<sub>0.75</sub>Mn<sub>0.75</sub>Al<sub>0.25</sub>O<sub>2</sub> cathode materials (marked by star and triangle symbols, respectively, in Fig. S1) where Mn is in a mixed oxidation state [18, 47]. As the presence of Jahn-Teller active Mn<sup>3+</sup> is considered detrimental to cyclic performance, structural and electrochemical analysis in monophasic and biphasic P2/P3 samples along the *'zero Mn<sup>3+</sup> line'* is crucial in identifying compositions with desired electrochemical properties in the Na<sub>3/4</sub>(Mn-Al-Ni)O<sub>2</sub> system. This approach can be extended to other composition phase diagrams involving Jahn-Teller active cations in selecting electrode materials with superior performance.

### 2. Materials and Methods

The cathode materials were synthesized using the sol-gel method. Stoichiometric quantities of manganese (II) acetate tetrahydrate, nickel acetate tetrahydrate, aluminum nitrate nonahydrate, and sodium carbonate were dissolved in deionized water, followed by the addition of ethylene glycol and citric acid. The homogeneous solution was then heated to form a gel, which was subsequently dried, heat treated, and calcinated at different temperatures (600 - 900 °C) to obtain the final product. The Al substituted series of compounds  $Na_{\frac{3}{4}}Mn_{\frac{5}{8}}Ni_{\frac{3}{8}}O_{2}$ ,  $Na_{\frac{3}{4}}Mn_{\frac{4.75}{8}}Al_{\frac{1.5}{8}}Ni_{\frac{2.75}{8}}O_{2}$ ,  $Na_{\frac{3}{4}}Mn_{\frac{4.55}{8}}Al_{\frac{1.5}{8}}Ni_{\frac{2.25}{8}}O_{2}$ , and  $Na_{\frac{3}{4}}Mn_{\frac{1}{2}}Al_{\frac{1}{4}}Ni_{\frac{1}{4}}O_{2}$ , (general composition  $Na_{\frac{3}{4}}Mn_{\frac{5-x}{8}}Al_{\frac{2x}{8}}Ni_{\frac{3-x}{8}}O_{2}$ , where x = 0, 0.25, 0.50, 0.75, and 1) synthesized for the study will henceforth be abbreviated as A0, A1, A2, A3, and A4, respectively (also see Table 1 for details).

The powder x-ray diffraction (XRD) patterns were obtained using a Malvern Pan Analytical Empyrean diffractometer (Cu-Kα radiation source) at room temperature. The XRD data was

analyzed using the *TOPAS Academic* (version 6) software package [48]. The morphological studies of the samples were conducted using a JEOL field emission scanning electron microscope (model JEOL-7610) equipped with energy-dispersive x-ray spectroscopy (EDS) for elemental mapping. The oxidation states of transition metal ions were studied using their X-ray photoelectron spectra (XPS), collected from a Thermofisher Scientific -Naxsa base with an Al Kα X-ray source (1486.6 eV). The x-ray absorption near edge structure (XANES) and extended x-ray absorption fine structure (EXAFS) experiments obtained at the Mn and Ni K-edge were carried out at scanning EXAFS beamline (BL-9) at Indus-2 synchrotron source (2.5 GeV, 150 mA) at Raja Ramanna Centre for Advanced Technology (RRCAT) Indore, India. The XANES and EXAFS data were analyzed using ATHENA and ARTEMIS software packages [49]. Operando Synchrotron XRD patterns were collected at the extreme conditions angle dispersive/energy dispersive synchrotron X-ray diffraction beamline (BL11) at Indus-2 (RRCAT) with a beam wavelength of 0.8312 Å and beam energy of 2.5 GeV.

The electrochemical experiments were conducted on CR2032 coin cells containing Na metal anode, 1M NaClO<sub>4</sub> in Propylene Carbonate electrolyte, and a Whatman GF/D filter paper separator. The cathode was prepared by coating a mixture of active material, Ketjen black, and PVDF (in a wt. ratio of 75:10:15) onto an Al current collector. Electrochemical experiments such as galvanostatic charge-discharge (GCD) tests and the galvanostatic intermittent titration technique (GITT) were carried out using a Neware battery tester (CT-4008T). The mass loading for the samples was ~ 4-5 mg cm<sup>-2</sup>, and C-rates were calculated, taking the nominal capacity of 150 mAh g<sup>-1</sup> (assuming a Na<sup>+</sup> extraction of 0.60). An NF Corp LCR meter (model: ZM 2376) was used to obtain the impedance data in the 1 Hz – 1 MHz frequency range at room temperature.

 Table 1. Details of the composition and phase-type for various samples prepared in the study.

Composition	Phase type	Label
$\begin{array}{ccc} \text{Na}_{\frac{3}{4}}\text{Mn}_{\frac{5}{8}}\text{Ni}_{\frac{3}{8}}\text{O}_{2} & & \\ & & \\ & & & \\ & & \\ & & & \\ & & \\ & & & \\ & \\ & & \\ & & \\ & & \\ & & \\ & & \\ & & \\ & & \\ & & \\ & & \\ & & \\ & & \\ & &$	Р3	A0- 1
	P3+P2	A0- 2
	P2	A0- 3
$Na_{\frac{3}{4}}Mn_{\frac{4.75}{8}}Al_{\frac{0.5}{8}}Ni_{\frac{2.75}{8}}O_{2}$	Р3	A1- 1
	P3+P2	A1- 2
	P2	A1- 3
$\begin{array}{c c} Na_{\frac{3}{4}}Mn_{\frac{4.5}{8}}Al_{\frac{1}{8}}Ni_{\frac{2.5}{8}}O_{2} & \\ & \end{array}$	Р3	A2- 1
	P3+P2	A2- 2
	P2	A2- 3
$Na_{\frac{3}{4}}Mn_{\frac{4.25}{8}}Al_{\frac{1.5}{8}}Ni_{\frac{2.25}{8}}O_{2}$	Р3	A3- 1
	P3+P2	A3- 2
	P2	A3- 3
$\begin{array}{c ccccccccccccccccccccccccccccccccccc$	Р3	A4- 1
	P3+P2	A4- 2
	P2	A4- 3

#### 3. Results and Discussion

#### 3.1. Structural characterization

A series of Al-substituted  $Na_{\frac{3}{4}}Mn_{\frac{5-x}{8}}Al_{\frac{2x}{8}}Ni_{\frac{3-x}{8}}O_{2}$  (x=0, 0.25, 0.50, 0.75, and 1) were synthesized through the sol-gel route. All these compositions (A0-A4) lie on the 'zero  $Mn^{3+}$  line' in the Mn-Ni-Al pseudo-ternary diagram where the concentration of  $Mn^{3+}$  is 0, as illustrated in Fig. 1. All compositions were synthesized with three intended phase structures: monophasic P3 (denoted as -1), monophasic P2 (denoted as -2), and biphasic P3/P2 (denoted as -3). For example, the P3 and P2 phases of A0 are denoted as A0-1 and A0-3, respectively, and the P3/P2 biphasic A0 will be denoted as A0-2.

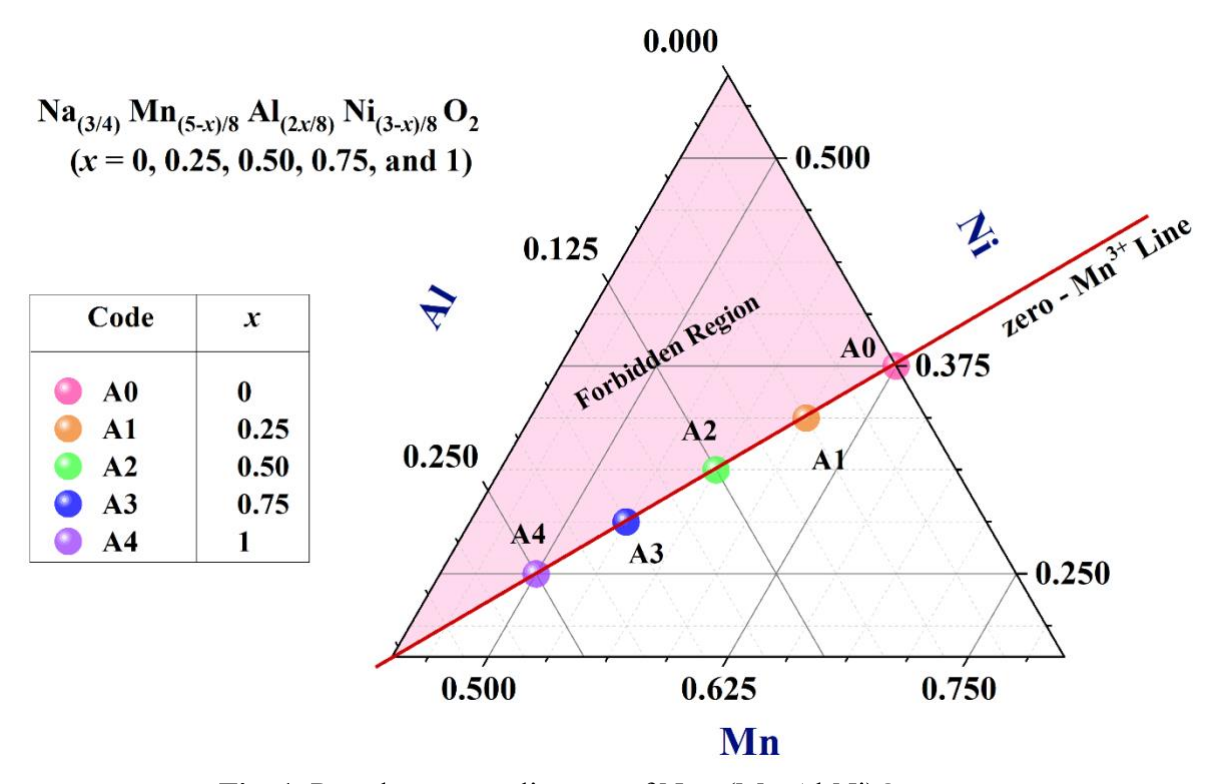


**Fig. 1.** Pseudo-ternary diagram of Na<sub>3/4</sub>(Mn-Al-Ni)O<sub>2</sub> system.

Fig. S2 illustrates the phase evolution of the A0 to A4 series of compounds with calcination temperature. The figure shows that the P3 phase in all 5 compositions formed at 650 °C, and as the calcination temperature increased, peaks consistent with a P2 phase started to emerge while the intensity of those corresponding to the P3 phase decreased. Another noticeable

feature of Fig. S2 is that the complete transformation of all the materials to a P2 type phase occurs at different temperatures. For A4 (which has the highest, i.e., 0.25, Al content), a monophasic P2 phase (A4-3) is obtained at 900 °C. In contrast, in other compositions with lower levels of Al<sup>3+</sup>, like in the case of A2 and A0, a pure P2 phase was obtained at relatively lower temperatures of 850 °C and 825 °C, respectively. Accordingly, the calcination temperatures for biphasic A2-2 and A0-2 were also lower than A4-2.

The changes to crystallographic parameters in the P3 and P2 phases in the A0-A4 series of compounds were analyzed using Rietveld refinement of room temperature XRD data (Fig. 2 and Fig. S3-S6). The refinement confirmed the existence of a single P3 phase (*R3m* space group) in all samples at 650 °C. With an increase in temperature, the intensities of (101), (102), and (105) peaks belonging to the P3 phase decline while (100), (102), and (103) peaks belonging to the P2 phase (*P63/mmc* space group) become prominent. Table S1-S5

displays the crystallographic parameters of the A0-A4 series of compounds obtained after Rietveld refinement of XRD data. Interestingly, the P3 and P2 unit cell volumes were found to be  $\sim 121~\text{Å}^3$  and 80.5 ų across all compositions. On the other hand, TM-O<sub>6</sub> octahedral volume in P3 and P2 type structures decreased from  $\sim 10.92~\text{Å}^3$  and  $10.90~\text{Å}^3$  in A0 to  $\sim 9.67~\text{Å}^3$  and  $10.05~\text{Å}^3$  in A4 while the volume of Na-O<sub>6</sub> prism increased from 11.98 ų and 11.91 ų in the former to 12.90 ų and 12.59 ų in latter. As a result, Na ion conduction bottlenecks (area of the rectangular face of Na-O<sub>6</sub> prism) are also bigger in A4.

The contraction of the TM-O<sub>2</sub> layers with an increase in Al concentration was further confirmed by the fitting of EXAFS data obtained at the Mn K-edge (Fig. S7). The Fourier transform fits of Mn K-edge in P3 and P2 type A0-A4 samples show decreasing Mn-O bond lengths from 2.01 Å (for P2 and P3) in A0 to 1.94 Å (P3) and 1.96 Å (P2) in A4. The decrease in effective TM-O bond length could be due to a higher bond strength of Al-O bonds

(511 kJ mol<sup>-1</sup>) compared to Ni-O (382 kJ mol<sup>-1</sup>) and Mn-O (401 kJ mol<sup>-1</sup>) bonds, which lowers the effective TM-O bond lengths in P3 and P2 layered oxide compounds, allowing the TM-O<sub>6</sub> octahedra to shrink with an increase in Al content [50]. Such alterations to TM-O<sub>2</sub> layers in layered oxide materials have also been reported in the Na-Mn-O system of cathode materials, where similar reductions in TM-O<sub>6</sub> octahedral volume were reported with Al substitution [38]. The higher bottleneck area in A4 compared to A0 could also lower the Na<sup>+</sup> migration energy with the material, which would help enhance its rate performance.

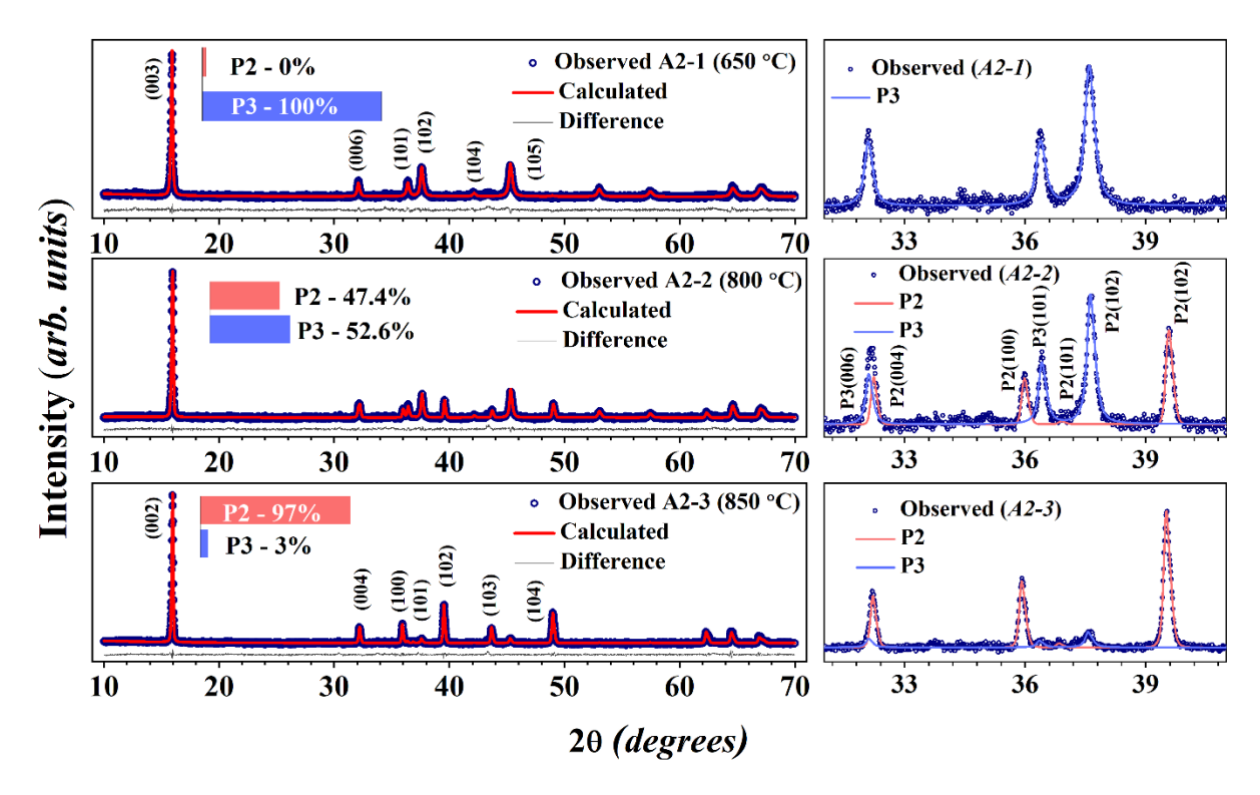


**Fig. 2.** Rietveld refinement of XRD data for A2-1, A2-2, and A2-3 samples, along with their deconvoluted P2 and P3 phases.

The morphological and microstructural studies of the A0-A4 series were carried out using FESEM. Fig. 3(a-c) portrays the SEM micrographs of A2-1,2,3, while the SEM images of A0, A1, A3, and A4 series of compounds are displayed in Fig. S8. The SEM micrographs reveal an increase in particle agglomeration with increased calcination temperature. The

monophasic P3 type materials of all compounds show smaller particles with spheroid shape. In comparison, the biphasic P3/P2 type materials can be observed to have bigger particles with a slightly higher degree of agglomeration. Samples with smaller particles and a relatively lower degree of agglomeration are preferred in cathode materials as they usually tend to show better rate performance and cyclic stabilities [51, 52]. In this regard, the P2 type compounds that exhibit highly agglomerated particle clusters may show degradations in specific capacities at higher C rates. The elemental mapping of A2-2 displayed in Fig. 3(b1-b5) confirms a homogeneous distribution of all the constituent elements.

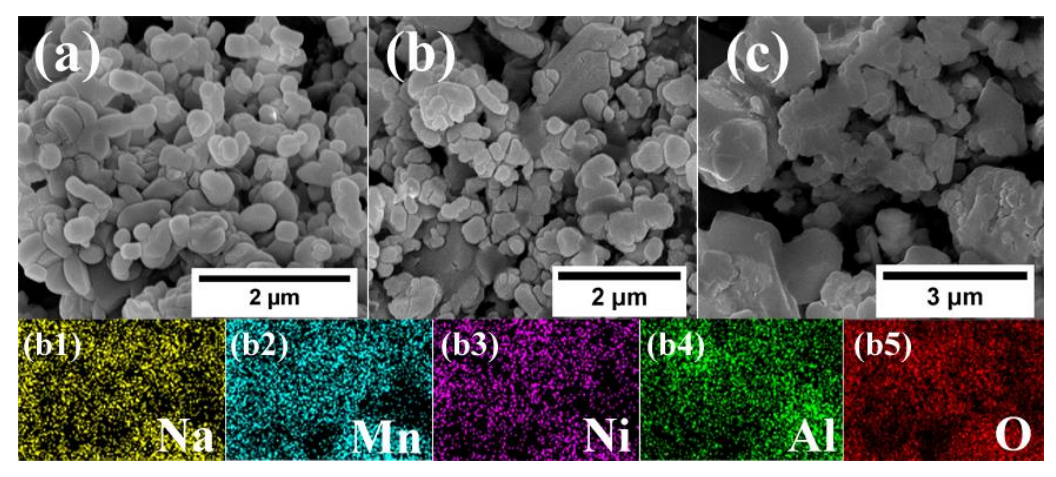


**Fig. 3.** SEM micrographs of (a) A2-1, (b) A2-2, and (c) A2-3 samples with (b1-5) representing the elemental maps of different elements in A2-2.

A combination of X-ray absorption near-edge spectra (XANES) obtained at the Mn K-edge and Mn 2p X-ray photoelectron spectra (XPS) was used to analyze the oxidation state of Mn ions in the as-synthesized A0-A4 series of materials. In Mn K-edge XANES spectra (Fig. 4(a)), the peak energies of all the compositions coincide at ~ 6561 eV, which indicates a 4+ oxidation state of Mn ions in these samples [53-56]. Similar conclusions are drawn from the Mn 2p spectra (Fig. 4(b)), which can be deconvoluted into 2 peaks at 643.2 and 654.7 eV, suggesting the presence of only Mn<sup>4+</sup> in these samples [57-59]. The oxidation state of Ni ions was identified by analyzing Ni 2p XPS spectra (Fig. S9), where the peaks at 854.26 and 871.75 eV confirmed a 2+ oxidation state of Ni ions in all samples [57-59]. The 4+ oxidation

state of Mn ions is a highly desirable feature in layered oxide cathodes that boosts their cyclic stability. Confirming the absence of Jahn-Teller active Mn<sup>3+</sup> has tremendous implications on the structural stability of the cathode materials during cycling, ensuring better cyclic performance.

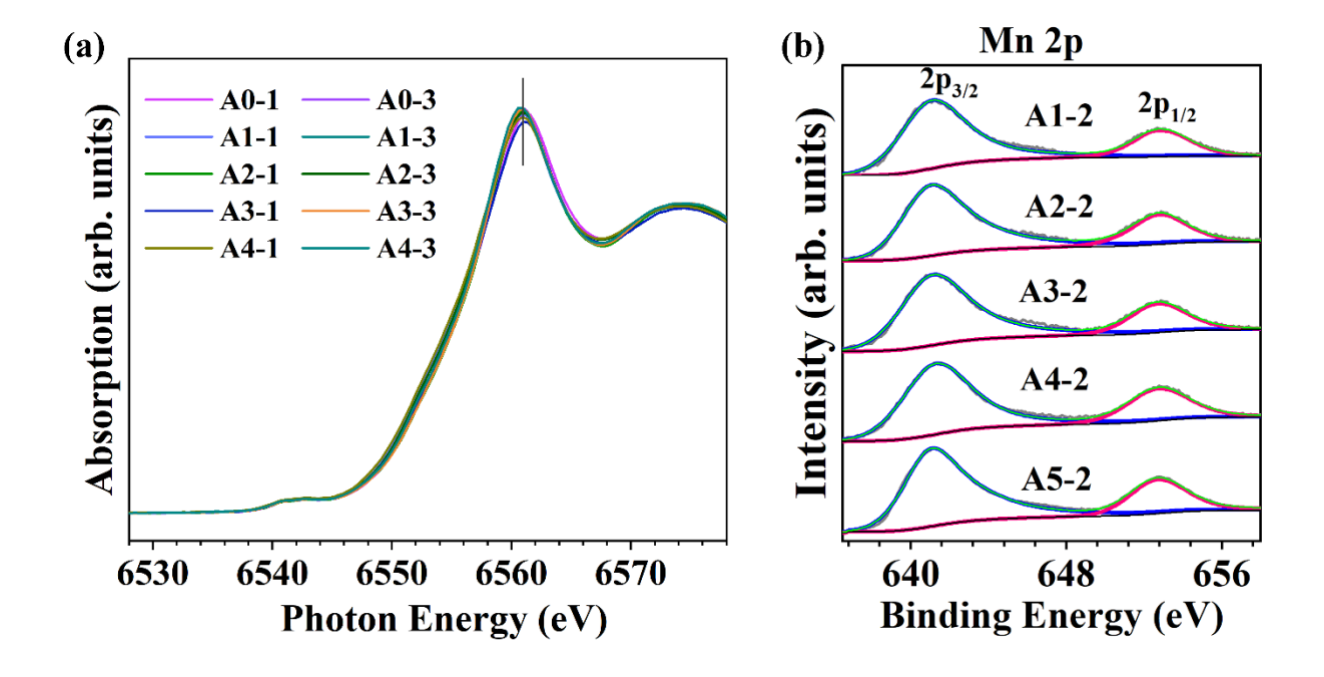


**Fig. 4.** (a) XANES spectra of A0-A4 samples taken at Mn Kedge with relevant standard compounds. (b) Mn 2p XPS plots of A0-2 to A4-2 compounds.

## 3.2. Electrochemical properties

The impacts of Al content and different P3/P2 phase fractions on electrochemical characteristics were analyzed by varying the charge-discharge rate between 0.1C and 6C in a 1.5-4.2 V range. Fig. 5 portrays the charge-discharge curves of A2-1, A2-2, and A2-3 along with their corresponding dQ/dV vs. Voltage plots at 0.1C, while the same for A0, A1, A3, and A4 series of samples are displayed in Fig. S10-S13. Interestingly, despite the decrease in the concentration of Ni<sup>2+</sup> active ions from A0 to A4, P3 type cathodes in all compositions (i.e., A0-1, A1-1, A2-1, A3-1, and A4-1) showed similar capacities close to 200 mAh g<sup>-1</sup> at 0.1C, which is equivalent to the extraction of ~ 0.8 Na<sup>+</sup> from each formula unit cell. Concurrently,

all the biphasic P3/P2 and monophasic P2 type cathodes also exhibited similar specific capacities close to 175 mAh g<sup>-1</sup> and 155 mAh g<sup>-1</sup>, respectively. This suggests an increase in the activity of Mn<sup>4+</sup> from A0-A4, as evidenced by the increase in the broadness of redox peaks below 2.5 V in the dQ/dV vs. Voltage (V) plots from A0 to A4, compensating for the decrease in Ni content (the redox peaks above 3 V in dQ/dV vs. Voltage plots are attributed to Ni<sup>3+/4+</sup> redox couples).

Further, the activity of Mn<sup>3+/4+</sup> redox couples also point to an increase in Na content in the cathode materials beyond 0.75. Hence, the specific capacities obtained at 0.1C between 1.5-4.2 V may not be realistic in a full-cell configuration. A possible solution to this problem would be to explore layered oxide cathodes with high Na or to limit the voltage window to 2.0-4.2 V, where Mn activity can be constrained. Limiting the voltage window to 2 V would cause an obvious reduction in specific capacity (up to 40% in A3 and A4 samples). Nevertheless, A3 and A4 cathodes possess larger Na<sup>+</sup> conduction bottleneck areas that facilitate superior rate performance and cyclic stability and can be employed in batteries for stationary storage applications. The decrease in specific capacity observed with an increase in P2 phase fraction is also widely reported in the literature. This is due to the inability of the P2 phase to accommodate a higher number of Na-ions [24-26]. In contrast, P3 phases can circumvent this problem by readily transforming into an O3 phase, typically when the concentration of Na<sup>+</sup> exceeds 0.75. Similar differences in specific capacities between P2 and P3 phases and superior performance of the P2/P3 mixed phase at high C rates in Mn/Ni-based layered oxide cathodes have also been reported previously [18, 47].

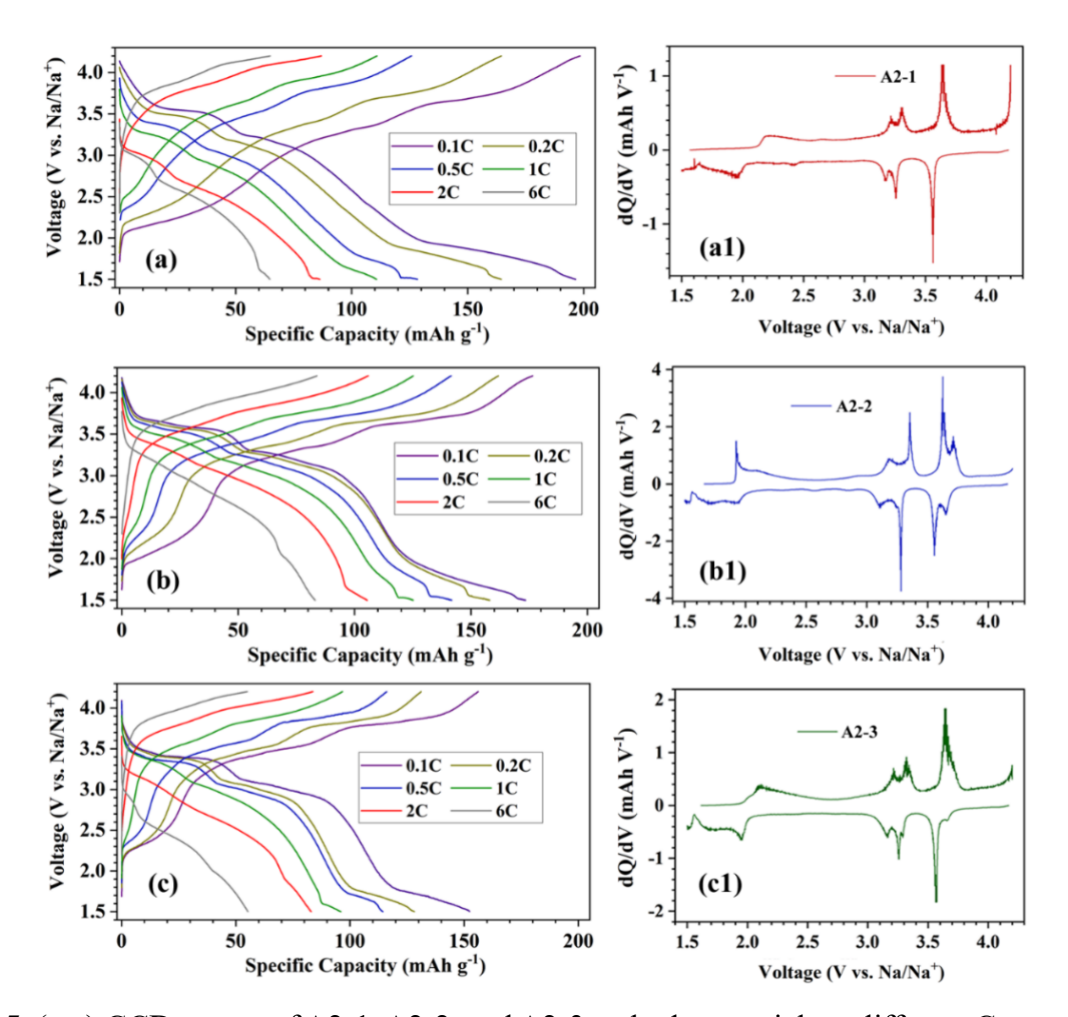


**Fig. 5.** (a-c) GCD curves of A2-1, A2-2, and A2-3 cathode materials at different C rates with (a1-c1) showing their respective dQ/dV vs. voltage (V) plots at 0.1C.

To study the rate performance behavior, GCD tests were conducted at different C-rates. Fig. 6(a), 6(b), and 6(c) represent the specific capacities of P3, biphasic P2/P3, and P2 samples for all compositions, respectively. The biphasic samples for all compositions (except A4) show better specific capacity at higher C-rates than their monophasic counterparts. In P3 type cathodes, A4-1 shows the highest rate performance, with discharge capacities close to 125 mAh g<sup>-1</sup> and 77 mAh g<sup>-1</sup> at 1C and 6C, respectively. This was closely followed by the A3-1, which exhibited specific capacities close to 120 mAh g<sup>-1</sup> and 66 mAh g<sup>-1</sup> at 1C and 6C, respectively. The superior rate performance of A4-1 and A3-1 concurs with the conclusions drawn from XRD data, where a higher Na<sup>+</sup> conduction bottleneck area was observed with increased Al content. In contrast, Al-substituted P2 type cathodes (A1-A4) show higher

degradation in specific capacities during cycling. This could be attributed to the higher agglomeration of particles observed in the P2 type materials reported earlier.

Contrary to the trend observed in P3 type cathodes, the rate performed of the P3/P2 biphasic cathode materials (Fig. 6(b)) initially improved with an increase in Al content till A1-2 and then decreased till A4-2. The P3/P2 biphasic A2-2 cathodes exhibited exceptional rate performance, delivering a specific capacity of 125 mAh g<sup>-1</sup> and 91 mAh g<sup>-1</sup> at 1C and 6C, respectively. At the same time, the initial enhancement in rate performance with an increase in Al content can be attributed to the increasing area of Na<sup>+</sup> conduction bottlenecks, with further increase in Al content, drastic reduction in electronic conduction due to the presence of a high concentration of inactive Al<sup>3+</sup>. This inevitably became the bottleneck limiting Na<sup>+</sup> extraction from the cathode materials, leading to inferior rate performance in A3-2 and A4-2. Since such a reduction in rate performances was not observed in the P3 type cathodes, the size of the cathode particles may have played a pivotal role in boosting their electronic conductivities. The Ketjen black additive mixed with the cathode slurry (to boost electronic conduction) is more effective in enhancing the electronic conductivity of the cathode layer containing smaller P3 phase particles (compensating for the decrease in electronic conductivity of P3 cathodes with high Al content) than in the larger and much more agglomerated P3/P2 cathodes.

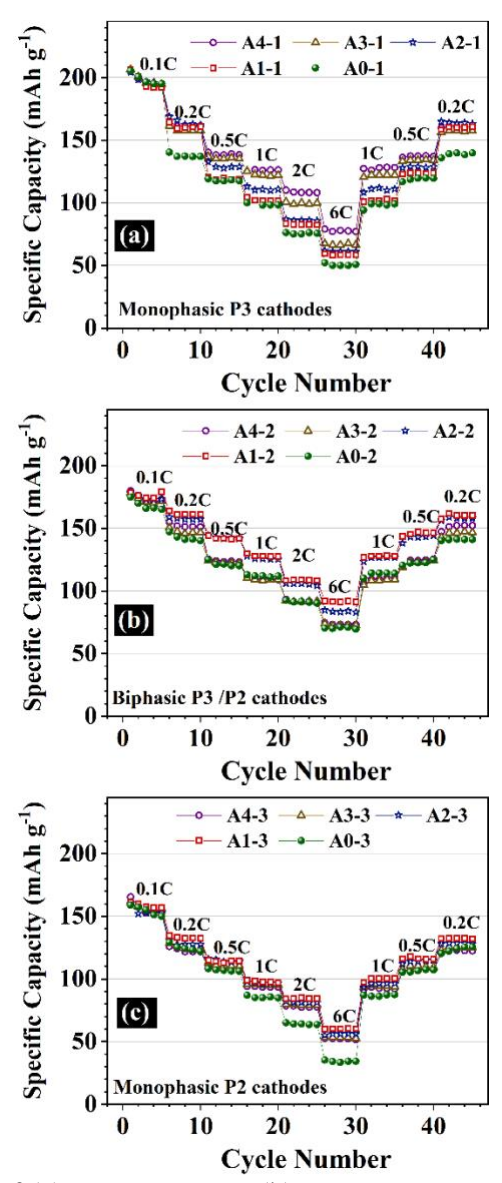


**Fig. 6.** Rate performance of (a) A0-1 to A4-1, (b) A0-2 to A4-2, and (c) A0-3 to A4-3 series of cathodes cycled between 1.5-4.2 V.

To evaluate the effect of Mn<sup>3+/4+</sup> redox couples on the cyclic performance of the cathodes, the cells were cycled between two different voltage windows: 1.5-4.2 V and 2.0-4.0 V (Mn<sup>3+/4+</sup> redox couples are largely active below 2.0 V). In the 1.5-4.2 V voltage window (Fig. 7(a1-a3)), the cyclic stability of the biphasic cathode materials in all five compositions is higher than their respective monophasic P3 and P2 counterparts. The superior cyclic performance of the biphasic cathode materials is attributed to the synergistic effect (manifested due to the

coexistence of two phases) that stabilizes both the P3 and P2 type structures, preventing phase transitions and large volume changes during cycling [30, 31, 47].

With an increase in the Al content, the cyclic stability shows rapid improvement initially, with A1-2 and A2-2 exhibiting about 68% and 78% capacity retention after 300 cycles compared to just 50% in A0-2. However, with a further increase in Al content beyond A2-2, capacity retention drops back to 68% in A4-2. The poor cyclic stability could be attributed to the increasing activity of Mn<sup>3+/4+</sup> redox couples (known to degrade structural stability) in the A4 and A3 compositions. Additionally, in the unsubstituted cathode samples (A0), the cyclic performance curves show a rapid decay in specific capacity after only a few cycles of steady performance, consistent with rapid structural degradation with cycling. This appears to have been remedied in the Al-substituted samples, where the capacity degradation appears gradual, suggesting improved structural stability with the substitution of Al<sup>3+</sup> for Mn<sup>4+</sup> and Ni<sup>2+</sup>. After limiting the voltage window to 2.0-4.0 V (Fig. 7(b1-b3)), A2-2 still delivered an impressive capacity of 99 mAh g<sup>-1</sup> at 1C and retained 87% of the initial capacity after 500 cycles. This is a substantial improvement over the unsubstituted biphasic A0-2, which exhibits a capacity retention of only 55% after 500 cycles. The monophasic P2 and P3 type A2 cathodes (Fig. 7(b2)) also showed higher cyclic performance, retaining up to 78% of their original capacity after 500 cycles. In higher Al substituted samples, A4-2 showed capacity retention of 78%, dropping from 87 mAh g<sup>-1</sup> to 66 mAh g<sup>-1</sup> after 500 cycles. Liming the lower cutoff voltage to  $2~\mathrm{V}$  limited the activity of the  $\mathrm{Mn}^{3+/4+}$  redox couple, which improved the cyclic performance of all the cathode materials. Further, as illustrated in Table S6, the cyclic performance achieved by the A2-2 cathode in this study is exceptionally higher than other A1-substituted layered oxide cathodes in literature, underling the importance of the 'zero Mn<sup>3+</sup> line' in identifying the optimum composition in Na<sub>3/4</sub>(Mn-Al-Ni)O<sub>2</sub> pseudo ternary system.

In the Nyquist plots in Fig. 8(a), A2-2 half cells show the lowest overall resistance  $\sim 300~\Omega$  and  $410~\Omega$  after 500 cycles (cycled between 2.0 to 4.0 V) and 300 cycles (cycled between 1.5 to 4.2 V), respectively. The analysis of EIS data using an equivalent circuit model revealed an increase in charge transfer resistance from  $\sim 170~\Omega$  in the fresh cells to 387  $\Omega$  after 500 cycles (in the 2.0-4.0 V range) and to 587  $\Omega$  after 300 cycles (in the 1.5-4.2 V range) for cell with A4-2 as the cathode. The charge transfer resistance increased to 260  $\Omega$  (after 500 cycles) and 354  $\Omega$  (after 300 cycles) in the half-cell with A2-2 cathode. The increase in charge transfer resistance of both the cells also indicates a higher degree of structural degradation in the materials when cycled in a wider voltage window. The lower charger transfer resistance in A2-2 also indicates the high structural durability of the cathode material.

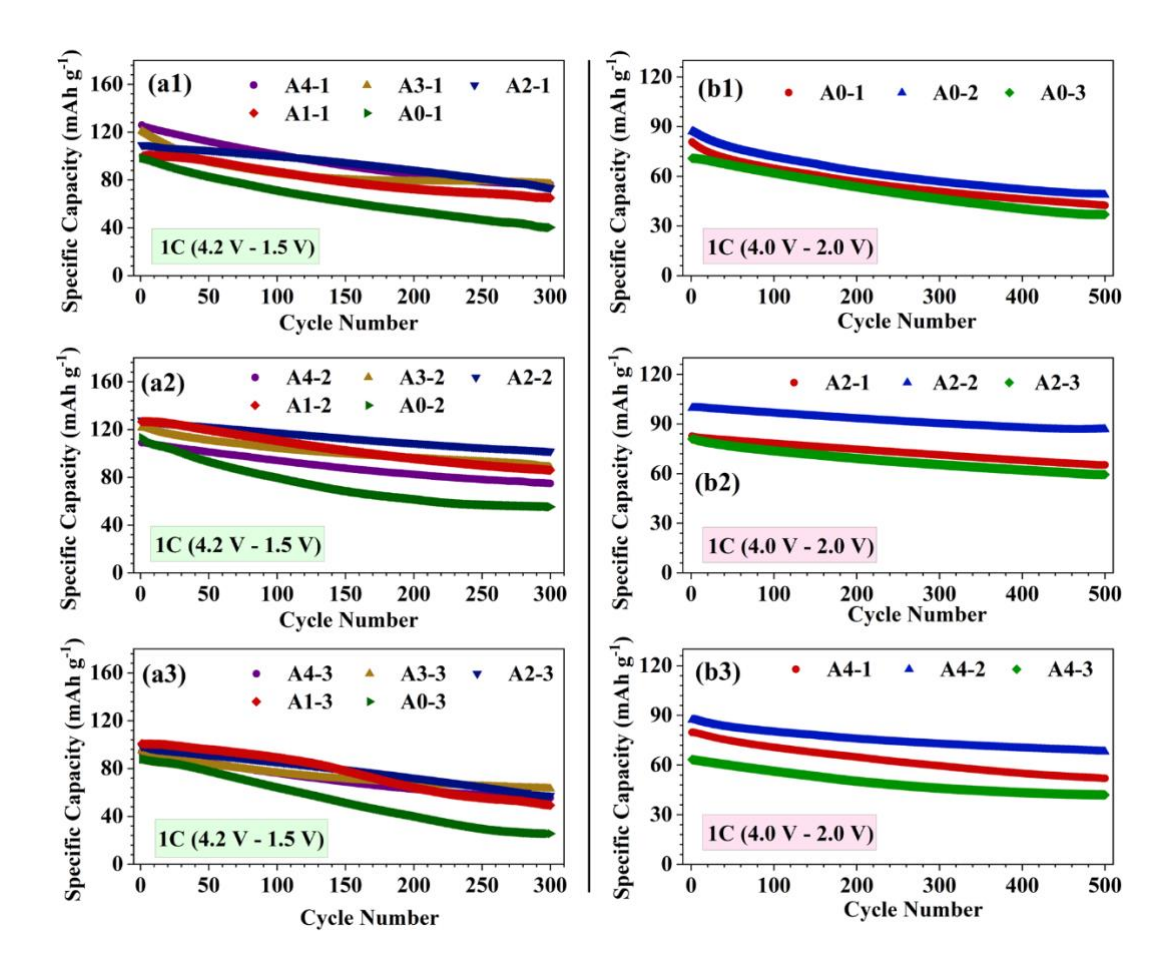


**Fig. 7.** Cyclic performance of A0-A4 series of cathodes at a discharge rate of 1C (a1-a3) betw een 1.5-4.2 V and (b1-b3) between 2.0-4.0 V.

As a result of the lower overall resistance, the A2-2 cell was also able to achieve a 94% energy efficiency during the initial cycles at 1C and still maintained an energy efficiency as high as 88% after 500 cycles (Fig. S14). Energy efficiency is vital to battery performance, often unreported in the literature. It determines the practical applicability of high-energy electrode materials and can also be used to diagnose various structural instabilities/variations (especially in interaction-type electrode materials) [60]. In the GCD curves plotted in Fig. S14, the overpotential seems to increase when the voltage drops below 3.0 V, indicating large-scale structural variations/transformations. Even at a high discharge rate of 1C, the high energy efficiency makes A2-2 a strong contender for commercialization in Na ion batteries.

The galvanostatic intermittent titration technique (GITT) was used to probe Na-ion kinematics in the A4, A2, and A0 series of compounds, and their resulting curves depicting the variation in Na<sup>+</sup> diffusion coefficients at different states of charge are displayed in Fig. 8(b), Fig. S15, and Fig. S16. As expected, in all the compounds, monophasic P3 and the biphasic P2/P3 biphasic cathodes show the lowest dispersion in diffusion coefficients at different states of charge compared to the P2 type cathode. In A2, the highest diffusion coefficient is observed in A2-2 ( $4.0 \times 10^{-10}$  cm<sup>2</sup> s<sup>-1</sup>) type cathode, while in A1, the highest diffusion coefficient is observed in A4-1 ( $4.0 \times 10^{-10}$  cm<sup>2</sup> s<sup>-1</sup>) which concurs with the rate performance results.

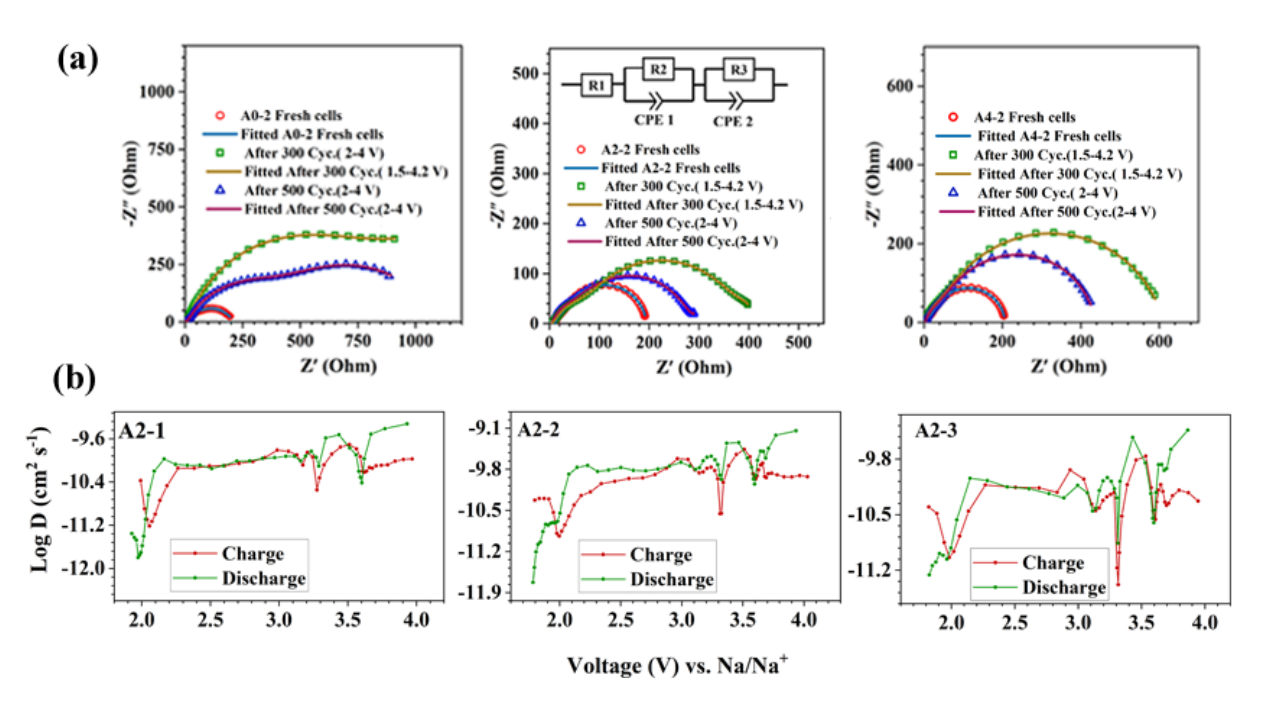


**Fig. 8.** (a) Nyquist plots of A0-2, A2-2, and A4-2 cathodes before and after cycling. Figure inset shows the equivalent circuit used to fit the impedance data. (b) Variation of diffusion coefficients of A0-2, A2-2, and A4-3 cathodes during a charge/discharge cycle.

The remarkable electrochemical performance of the A2-2 cathode prompted us to further test the material in a full-cell configuration with a hard carbon anode. The hard carbon was presodiated before being assembled into the full cell; the charge-discharge cycle of hard carbon is shown in Fig. S17. During electrochemical tests, the A2-2 full cell exhibited a specific capacity of 104 mAh g<sup>-1</sup> (~ 90% capacity of A2-2 half cell) between 2.0-4.0 V at a charge/discharge rate of 0.2C and retained 90% of its initial specific capacity after 100 cycles (Fig. S18).

## 3.3. Operando Synchrotron XRD.

The improved structural stability of the Al-substituted cathodes and the adverse effects of Mn<sup>3+/4+</sup> redox couples on the layered oxide structure were confirmed using operando Synchrotron XRD of cathode materials. The Synchrotron XRD patterns were obtained for the A2 and A4 series of cells while cycling at a charge/discharge rate of 0.1C between 1.5-4.2 V

(schematic of the operando XRD setup is shown in Fig. S19). Fig. 9(a-c) depicts the XRD patterns of A2-1, A2-2, and A2-3 cathode materials, and the same for A4-1, A4-2, and A4-3 are presented in Fig. S20. Initial analysis of the XRD patterns of both A2-1 and A4-1 confirmed our speculations about large variations in lattice parameters associated with the activation of  $Mn^{3+/4+}$  in layered oxide structures, as evidenced by the shift in the (003) peak to higher angles (signifying a shrinkage of unit cell along the c axis due to a decreased repulsion between  $O^{2-}$  with an increasing amount of  $Na^+$  in the unit cell) during the discharge cycle when the cell voltage falls below 2 V.

Further analysis using Le-Bail fitting (Fig. S21(a-c) and Fig. S22(a-c)) also revealed a peculiar feature in the XRD patterns of Al substituted P3 type samples where a complete absence of the O3 phase was observed even when the voltage reached 1.5 V. Even in the A4-1, where the Mn³+/4+ redox couples were largely active, Le-Bail fitting could find any peaks related to an O3 phase. As discussed in the previous section, the activation of Mn³+/4+ redox couples in the A1-A4 series of materials indicated an increase in Na content above 0.75, which would ideally trigger the P3-O3 phase transformations as reported in the literature, especially in A4-1 where Mn³+/4+ redox couples contributed close to 40% of its specific capacity [16, 19, 61-64]. Yet the complete absence of an O3 phase points to the ability of Alions to suppress the P3-O3 phase transformations in these samples. As Na<sup>+</sup> kinetics in the O3 phases is quite poor compared to the P3 and P2 type structures, the absence of the O3 phase also explains the comparatively high-rate performance of the A4-1 cathode.

In the P2 type structures, the activation of  $Mn^{3+/4+}$  redox couple not only causes large variations in the c parameter of the  $P6_3/mmc$  unit cell but also initiates phase transformation as evidenced by the presence of an extra peak next to the P2 (002) at  $\sim 7.5^{\circ}$  in Fig. 9(c) and Fig. S20(c). This was confirmed to be the (004) peak of a P'2 phase (C2/c space group) through Le-bail fitting of XRD patterns (Fig. S21(c) and Fig. S22(c)). P2 to P'2 phase

transformation has been reported in Na-Mn-Ni-based systems at low voltages [65, 66]. It is often described as an intermediatory phase that forms before the P2 type structure completely transforms into an OP4 phase. Contrary to the drastic structural variations and phase transformations observed in the P3 and P2 type cathodes, the operando-XRD patterns of the biphasic A2-2 and A4-2 cathode materials exhibit smoother structural variations throughout the entire charge/discharge cycle. The synergistic effects, widely reported in biphasic cathodes, appear to have stabilized both the P3 and P2 type structures in the material, preventing any unwanted phase transformations even at voltages, which may very well have led to their impressive electrochemical performance [30, 31, 47, 67]. As prominent structural changes observed in Fig. 9 and S20 occur when the cell is discharged below 2.0 V, restricting the charge-discharge voltage window to 2.0-4.0 V improves the cycling performance of all the samples quite significantly, as expected.

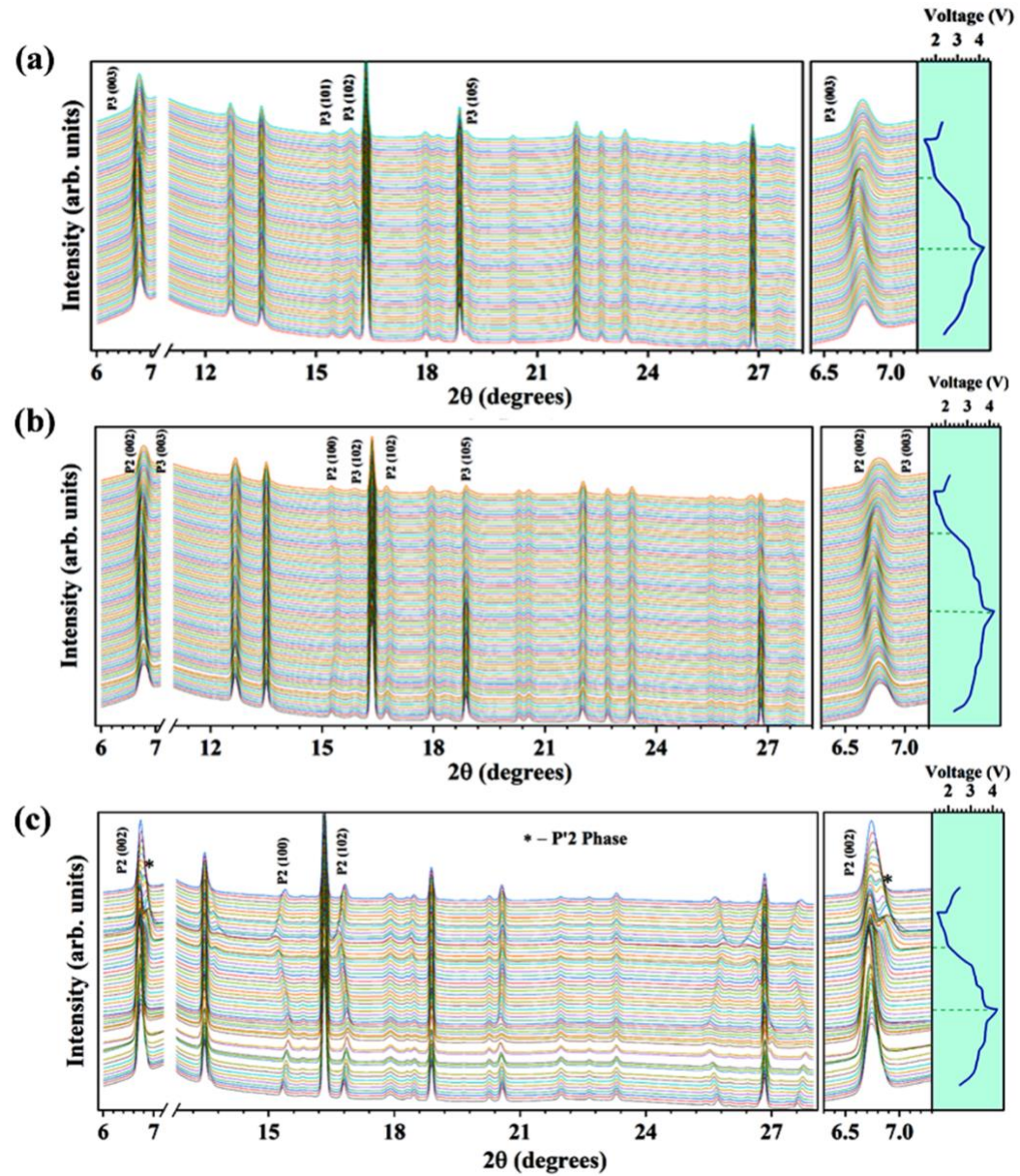


**Fig. 9.** Operando Synchrotron XRD patterns of half-cells employing (a) A2-1, (b) A2-2, and (c) A2-3 samples as cathodes collected during the first charge/discharge cycle.

To study the effect of Al substitution and the role of a biphasic cathode in structural stabilization, the variation in volume and lattice parameters of the hexagonal unit cells were quantified. The variations in the *c* parameter of all A2 and A4 cathodes (Fig. S23 and S24) follow a trend well documented in layered oxides where the unit cell expands and contracts along the *c* axis during charging and discharging [38, 65, 68]. The variation in volume of the A2 and A4 series of materials (Fig. S21(a1-c1) and Fig. S22(a1-c1)), on the other hand, shows a decrease in unit cell volume upon charging and expands during discharging. Table

S7 summarises the maximum percentage change in cell volume of P2 and P3 type phases in A4 and A2 monophasic and biphasic cathodes. As expected, the P3 and P2 phases in the A2-2 and A4-2 cathodes exhibited much lower variation in cell volume than their monophasic counterparts. In fact, the P3 and P2 structures in the A2-2 only expanded to about 0.9% and 0.8% of the minimum volumes, which makes it on par with some of the 'zero strain' cathodes reported in literature. Overall, biphasic P3/P2 cathode materials were found to have superior electrochemical performance compared to their monophasic P3 and P2 counterparts. Fig. 10 and Table S8 compare the various properties of all biphasic cathode materials. During electrochemical testing, A2-2 exhibited several outstanding electrochemical properties, such as high specific capacity, cyclability, and energy efficiency, characteristics that are highly sought after in cathodes for commercial applications.

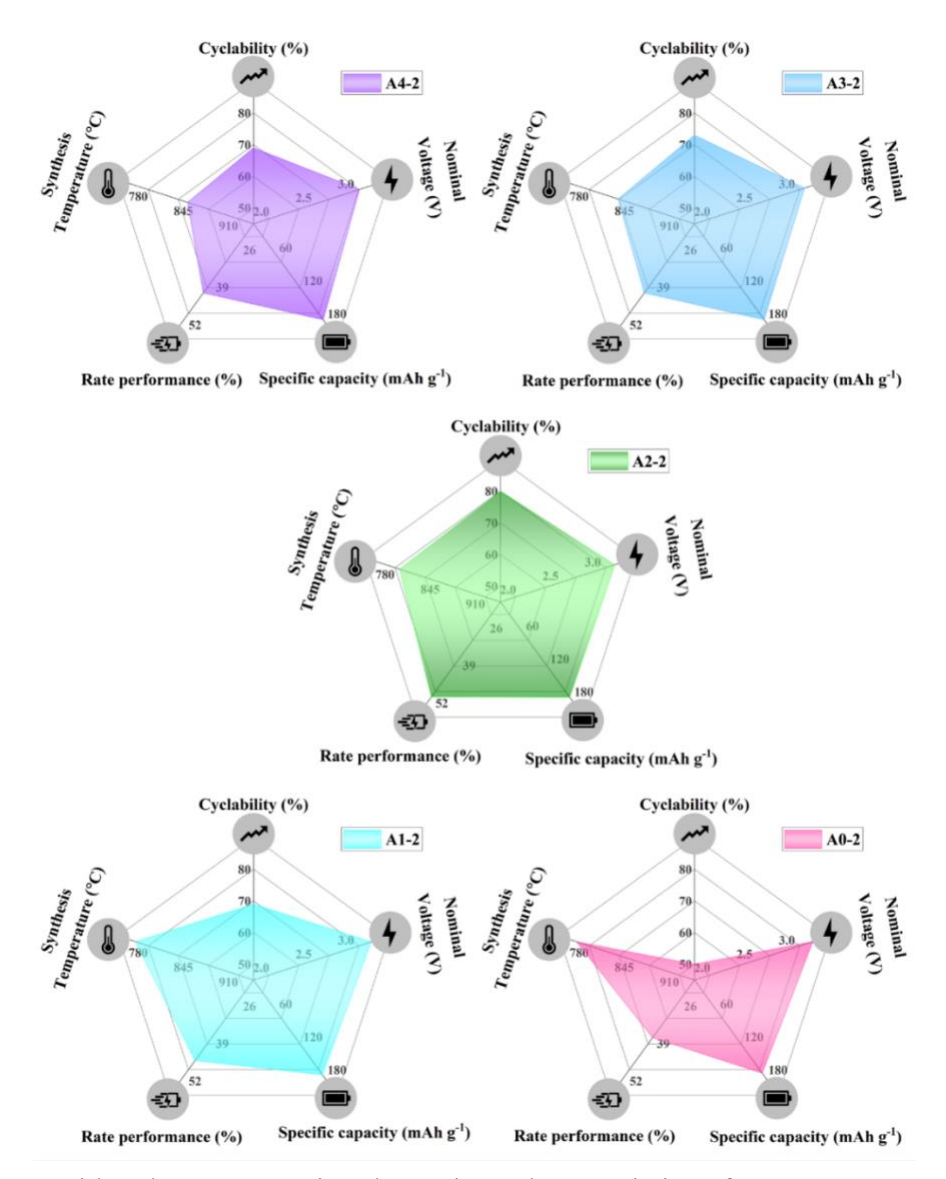


**Fig. 10.** Spider charts comparing the various characteristics of A0-2 to A4-2 cathode materials.

## 4. Conclusions

The series of Al-substituted Na $\frac{3}{4}$ Mn $\frac{5-x}{8}$ Al $\frac{2x}{8}$ Ni $\frac{3-x}{8}$ O $_2$  (x=0, 0.25, 0.50, 0.75, and 1) cathode materials lying along the 'zero  $Mn^{3+}$  line' were synthesized with varying P3/P2 phase fractions. Experimental data from XRD, EXAFS, and SEM techniques were used for structural analysis of the cathode materials. XRD data showed an increasing trend in calcination temperature for P2 phase formation in compounds with a higher Al concentration. The Rietveld refinement of XRD data showed a consistent increase in Na $^+$  conduction

bottleneck area in both P3 and P2 structures with increased Al concentration. Larger particle agglomeration was observed in the SEM micrographs of the P2 type cathodes calcinated at relatively higher temperatures. The absence of Mn<sup>3+</sup> was confirmed through XANES and XPS spectra of the A0-A4 series of cathode materials, which showed the presence of only Mn<sup>4+</sup> in the materials. The electrochemical performance of the cathode samples was evaluated between 1.5-4.2V and 2.0-4.0 V voltage windows. The P3 type cathodes showed a high specific capacity of ~ 195 mAh g<sup>-1</sup>, which decreased with increased P2 phase concentration. Compared to the Na<sub>0.75</sub>Mn<sub>0.625</sub>Ni<sub>0.375</sub>O<sub>2</sub> cathode (A0), the Al-substituted samples exhibited significantly higher rate performance and cyclic stability. It was also observed that, within each composition, the biphasic cathode with  $\sim 50\%$  P3 and  $\sim 50\%$  P2 phase fractions outperformed their monophasic counterparts in almost all electrochemical performance parameters. The biphasic A2 sample with 0.125 Al concentration, in particular, demonstrated excellent cyclic properties, retaining close to 78% of its initial specific capacity after 300 cycles at 1C between 1.5-4.2 V, which improved to 87% after 500 cycles when the cycling was limited in the 2.0-4.0 V voltage range. The material also exhibited about 88% energy efficiency after 500 cycles. Further, the full cell assembled with the biphasic A2 cathode showed only a 10% reduction in specific capacity compared to its half-cell and retained 90% capacity after 100 cycles at 0.2C. The remarkable electrochemical performance of the biphasic cathode was attributed to the synergistic effect of P3/P2 coexistence, which was found to suppress the volume expansion of both the P3 and P2 structures during cycling. Interestingly, operando Synchrotron XRD data from the P3 type phases revealed a persisting P3 phase in the monophasic Al substituted cathodes across the entire 1.5-4.2 V range. The absence of a P3 to O3 phase transformation may be due to the presence of A13+, which may also have been responsible for the considerably high rater performance in the P3 type cathodes. Additionally, Le-Bail fitting of synchrotron XRD data revealed the detrimental impact of activating Mn<sup>3+/4+</sup> redox couple in layered oxide structure. In P2 type cathodes, a P2 to P'2 phase transformation was observed, while in the P3 type phase, the unit cell was found to expand by 1.5% of its pristine volume when the cells were discharged below 2.0 V.

## Acknowledgments

SK thanks the Science and Engineering Research Board (SERB), Govt. of India, for the financial support (grant number: CRG/2021/005548). The authors acknowledge RRCAT and Dr. Biplab Ghosh for his help in recording the EXAFS spectra at RRCAT, Indore, India.

### **Declaration of Interest**

The authors declare no conflict of interests.

#### References

- [1] J.-M. Tarascon, Joule 4 (2020) 1616-1620 <a href="https://doi.org/10.1016/j.joule.2020.06.003">https://doi.org/10.1016/j.joule.2020.06.003</a>.
- [2] E. Goikolea, V. Palomares, S. Wang, I.R. de Larramendi, X. Guo, G. Wang, T. Rojo, Adv. Energy Mater. 10 (2020) 2002055 <a href="https://doi.org/10.1002/aenm.202002055">https://doi.org/10.1002/aenm.202002055</a>.
- [3] J. Darga, J. Lamb, A. Manthiram, Energy Technol. 8 (2020) 2000723 https://doi.org/10.1002/ente.202000723.
- [4] R.J. Clément, P.G. Bruce, C.P. Grey, J. Electrochem. Soc. 162 (2015) A2589-A2604 https://doi.org/10.1149/2.0201514jes.
- [5] R. Usiskin, Y. Lu, J. Popovic, M. Law, P. Balaya, Y.-S. Hu, J. Maier, Nature Rev. Mater. 6 (2021) 1020-1035 https://doi.org/10.1038/s41578-021-00324-w.
- [6] Y. Tian, G. Zeng, A. Rutt, T. Shi, H. Kim, J. Wang, J. Koettgen, Y. Sun, B. Ouyang, T. Chen, Z. Lun, Z. Rong, K. Persson, G. Ceder, Chem. Rev. 121 (2021) 1623-1669 https://doi.org/10.1021/acs.chemrev.0c00767.
- [7] T. Liu, B. Wang, X. Gu, L. Wang, M. Ling, G. Liu, D. Wang, S. Zhang, Nano Energy 30 (2016) 756-761 <a href="https://doi.org/10.1016/j.nanoen.2016.09.024">https://doi.org/10.1016/j.nanoen.2016.09.024</a>.
- [8] Y. Gupta, P. Siwatch, R. Karwasra, K. Sharma, S.K. Tripathi, Renew. Sust. Energ. Rev. 192 (2024) 114167 https://doi.org/10.1016/j.rser.2023.114167.
- [9] V. Palomares, P. Serras, I. Villaluenga, K.B. Hueso, J. Carretero-González, T. Rojo, Energy Environ. Sci. 5 (2012) 5884-5901 https://doi.org/10.1039/C2EE02781J.
- [10] C. Delmas, C. Fouassier, P. Hagenmuller, Physica B+C 99 (1980) 81-85 https://doi.org/10.1016/0378-4363(80)90214-4.
- [11] F. Wei, Q. Zhang, P. Zhang, W. Tian, K. Dai, L. Zhang, J. Mao, G. Shao, J. Electrochem.
  Soc. 168 (2021) 050524 https://doi.org/10.1149/1945-7111/abf9bf.

- [12] P.-F. Wang, Y. You, Y.-X. Yin, Y.-G. Guo, Adv. Energy Mater. 8 (2018) 1701912 https://doi.org/10.1002/aenm.201701912.
- [13] Y. Zhao, Q. Liu, X. Zhao, D. Mu, G. Tan, L. Li, R. Chen, F. Wu, Mater. Today 62 (2023) 271-295 <a href="https://doi.org/10.1016/j.mattod.2022.11.024">https://doi.org/10.1016/j.mattod.2022.11.024</a>.
- [14] T.-T. Wei, X. Liu, S.-J. Yang, P.-F. Wang, T.-F. Yi, J. Energy Chem. 80 (2023) 603-613 https://doi.org/10.1016/j.jechem.2023.02.016.
- [15] M. Jiang, G. Qian, X.-Z. Liao, Z. Ren, Q. Dong, D. Meng, G. Cui, S. Yuan, S.-J. Lee, T. Qin, X. Liu, Y. Shen, Y.-S. He, L. Chen, Y. Liu, L. Li, Z.-F. Ma, J. Energy Chem. 69 (2022) 16-25 <a href="https://doi.org/10.1016/j.jechem.2022.01.010">https://doi.org/10.1016/j.jechem.2022.01.010</a>.
- [16] L. Yu, Y.-X. Chang, M. Liu, Y.-H. Feng, D. Si, X. Zhu, X.-Z. Wang, P.-F. Wang, S. Xu, ACS Appl. Mater. Interfaces 15 (2023) 23236-23245 <a href="https://doi.org/10.1021/acsami.3c02514">https://doi.org/10.1021/acsami.3c02514</a>.
- [17] M. Sathiya, Q. Jacquet, M.-L. Doublet, O.M. Karakulina, J. Hadermann, J.-M. Tarascon, Adv. Energy Mater. 8 (2018) 1702599 <a href="https://doi.org/10.1002/aenm.201702599">https://doi.org/10.1002/aenm.201702599</a>.
- [18] H.N. Vasavan, M. Badole, S. Saxena, V. Srihari, A.K. Das, P. Gami, S. Deswal, P. Kumar, S. Kumar, Mater. Today Energy. 37 (2023) 101380 <a href="https://doi.org/10.1016/j.mtener.2023.101380">https://doi.org/10.1016/j.mtener.2023.101380</a>.
- [19] X.-M. Lin, X.-T. Yang, H.-N. Chen, Y.-L. Deng, W.-H. Chen, J.-C. Dong, Y.-M. Wei, J.-F. Li, J. Energy Chem. 76 (2023) 146-164 <a href="https://doi.org/10.1016/j.jechem.2022.09.016">https://doi.org/10.1016/j.jechem.2022.09.016</a>.
- [20] Y. Shi, Z. Zhang, P. Jiang, A. Gao, K. Li, Q. Zhang, Y. Sun, X. Lu, D. Cao, X. Lu, Energy Storage Mater. 37 (2021) 354-362 https://doi.org/10.1016/j.ensm.2021.02.020.
- [21] T. Risthaus, L. Chen, J. Wang, J. Li, D. Zhou, L. Zhang, D. Ning, X. Cao, X. Zhang, G. Schumacher, M. Winter, E. Paillard, J. Li, Chem. Mater. 31 (2019) 5376-5383 <a href="https://doi.org/10.1021/acs.chemmater.8b03270">https://doi.org/10.1021/acs.chemmater.8b03270</a>.

- [22] L. Xian, M. Li, D. Qiu, C. Qiu, C. Yue, F. Wang, R. Yang, J. Alloys Compd. 905 (2022) 163965 <a href="https://doi.org/10.1016/j.jallcom.2022.163965">https://doi.org/10.1016/j.jallcom.2022.163965</a>.
- [23] L. Yang, J.M.L. del Amo, Z. Shadike, S.-M. Bak, F. Bonilla, M. Galceran, P.K. Nayak, J.R. Buchheim, X.-Q. Yang, T. Rojo, P. Adelhelm, Adv. Funct. Mater. 30 (2020) 2003364 <a href="https://doi.org/10.1002/adfm.202003364">https://doi.org/10.1002/adfm.202003364</a>.
- [24] S. Saxena, H.N. Vasavan, M. Badole, A.K. Das, S. Deswal, P. Kumar, S. Kumar, J. Energy Storage 64 (2023) 107242 <a href="https://doi.org/10.1016/j.est.2023.107242">https://doi.org/10.1016/j.est.2023.107242</a>.
- [25] J. Feng, D. Fang, Z. Yang, J. Zhong, C. Zheng, Z. Wei, J. Li, J. Power Sources 553 (2023) 232292 <a href="https://doi.org/10.1016/j.jpowsour.2022.232292">https://doi.org/10.1016/j.jpowsour.2022.232292</a>.
- [26] C. Hakim, H.D. Asfaw, R. Younesi, D. Brandell, K. Edström, I. Saadoune, Electrochim. Acta 438 (2023) 141540 https://doi.org/10.1016/j.electacta.2022.141540.
- [27] H.N. Vasavan, M. Badole, S. Dwivedi, D. Kumar, P. Kumar, S. Kumar, Chem. Eng. J. 448 (2022) 137662 <a href="https://doi.org/10.1016/j.cej.2022.137662">https://doi.org/10.1016/j.cej.2022.137662</a>.
- [28] H.N. Vasavan, M. Badole, S. Saxena, A.K. Das, S. Deswal, P. Kumar, S. Kumar, ACS Appl. Energy Mater. 6 (2023) 2440-2447 https://doi.org/10.1021/acsaem.2c03750.
- [29] G. Liu, W. Xu, J. Wu, Y. Li, L. Chen, S. Li, Q. Ren, J. Wang, J. Energy Chem. 83 (2023) 53-61 https://doi.org/10.1016/j.jechem.2023.04.029.
- [30] X. Liang, T.-Y. Yu, H.-H. Ryu, Y.-K. Sun, Energy Storage Mater. 47 (2022) 515-525 https://doi.org/10.1016/j.ensm.2022.02.043.
- [31] E. Lee, J. Lu, Y. Ren, X. Luo, X. Zhang, J. Wen, D. Miller, A. DeWahl, S. Hackney, B. Key, D. Kim, M.D. Slater, C.S. Johnson, Adv. Energy Mater. 4 (2014) 1400458 <a href="https://doi.org/10.1002/aenm.201400458">https://doi.org/10.1002/aenm.201400458</a>.

- [32] Y.-N. Zhou, P.-F. Wang, Y.-B. Niu, Q. Li, X. Yu, Y.-X. Yin, S. Xu, Y.-G. Guo, Nano Energy 55 (2019) 143-150 <a href="https://doi.org/10.1016/j.nanoen.2018.10.072">https://doi.org/10.1016/j.nanoen.2018.10.072</a>.
- [33] C. Chen, B. Han, G. Lin, Q. Huang, S. Zhao, D. Zhang, C. Ma, D.G. Ivey, W. Wei, ACS Appl. Mater. Interfaces 10 (2018) 28719-28725 <a href="https://doi.org/10.1021/acsami.8b10519">https://doi.org/10.1021/acsami.8b10519</a>.
- [34] R. Li, J. Gao, J. Li, H. Huang, X. Li, W. Wang, L.-R. Zheng, S.-M. Hao, J. Qiu, W. Zhou, Adv. Funct. Mater. 32 (2022) 2205661 https://doi.org/10.1002/adfm.202205661.
- [35] X. Wu, J. Guo, D. Wang, G. Zhong, M.J. McDonald, Y. Yang, J. Power Sources 281 (2015) 18-26 https://doi.org/10.1016/j.jpowsour.2014.12.083.
- [36] M.H. Han, E. Gonzalo, N. Sharma, J.M. López del Amo, M. Armand, M. Avdeev, J.J. Saiz Garitaonandia, T. Rojo, Chem. Mater. 28 (2016) 106-116 <a href="https://doi.org/10.1021/acs.chemmater.5b03276">https://doi.org/10.1021/acs.chemmater.5b03276</a>.
- [37] Z. Cao, L. Li, C. Zhou, X. Ma, H. Wang, Funct. Mater. Lett. 13 (2020) 2051010 https://doi.org/10.1142/S1793604720510108.
- [38] X. Liu, W. Zuo, B. Zheng, Y. Xiang, K. Zhou, Z. Xiao, P. Shan, J. Shi, Q. Li, G. Zhong, R. Fu, Y. Yang, Angew. Chem. Int. Ed. 58 (2019) 18086-18095 <a href="https://doi.org/10.1002/anie.201911698">https://doi.org/10.1002/anie.201911698</a>.
- [39] G. Singh, N. Tapia-Ruiz, J.M. Lopez del Amo, U. Maitra, J.W. Somerville, A.R. Armstrong, J. Martinez de Ilarduya, T. Rojo, P.G. Bruce, Chem. Mater. 28 (2016) 5087-5094 <a href="https://doi.org/10.1021/acs.chemmater.6b01935">https://doi.org/10.1021/acs.chemmater.6b01935</a>.
- [40] T. Yang, Y. Huang, J. Zhang, H. Zhu, J. Ren, T. Li, L.C. Gallington, S. Lan, L. Yang, Q. Liu, J. Energy Chem. 73 (2022) 542-548 https://doi.org/10.1016/j.jechem.2022.06.016.
- [41] W.-L. Pang, X.-H. Zhang, J.-Z. Guo, J.-Y. Li, X. Yan, B.-H. Hou, H.-Y. Guan, X.-L. Wu, J. Power Sources 356 (2017) 80-88 <a href="https://doi.org/10.1016/j.jpowsour.2017.04.076">https://doi.org/10.1016/j.jpowsour.2017.04.076</a>.

- [42] A. Hebert, C. David, E. McCalla, ACS Appl. Energy Mater. 6 (2023) 4593-4603 https://doi.org/10.1021/acsaem.2c03994.
- [43] S.-T. Myung, F. Maglia, K.-J. Park, C.S. Yoon, P. Lamp, S.-J. Kim, Y.-K. Sun, ACS Energy Lett. 2 (2017) 196-223 <a href="https://doi.org/10.1021/acsenergylett.6b00594">https://doi.org/10.1021/acsenergylett.6b00594</a>.
- [44] A. Chakraborty, S. Kunnikuruvan, S. Kumar, B. Markovsky, D. Aurbach, M. Dixit, D.T. Major, Chem. Mater. 32 (2020) 915-952 <a href="https://doi.org/10.1021/acs.chemmater.9b04066">https://doi.org/10.1021/acs.chemmater.9b04066</a>.
- [45] S. Jia, J. Counsell, M. Adamič, A. Jonderian, E. McCalla, J. Mater. Chem. A 10 (2022) 251-265 <a href="http://dx.doi.org/10.1039/D1TA07940A">http://dx.doi.org/10.1039/D1TA07940A</a>.
- [46] J. Xu, J. Chen, K. Zhang, N. Li, L. Tao, C.-P. Wong, Nano Energy 78 (2020) 105142 https://doi.org/10.1016/j.nanoen.2020.105142.
- [47] H.N. Vasavan, M. Badole, S. Saxena, V. Srihari, A.K. Das, P. Gami, S. Deswal, P. Kumar, S. Kumar, J. Energy Storage 74 (2023) 109428 <a href="https://doi.org/10.1016/j.est.2023.109428">https://doi.org/10.1016/j.est.2023.109428</a>.
- [48] A. Coelho, J. Appl. Crystallogr. 51 (2018) 210-218 https://doi.org/10.1107/S1600576718000183.
- [49] B. Ravel, M. Newville, J. Synchrotron Radiat. 12 (2005) 537-541 https://doi.org/doi:10.1107/S0909049505012719.
- [50] L. Wang, B. Chen, J. Ma, G. Cui, L. Chen, Chem. Soc. Rev. 47 (2018) 6505-6602 http://dx.doi.org/10.1039/C8CS00322J.
- [51] Z. Zhang, R. Wang, J. Zeng, K. Shi, C. Zhu, X. Yan, Adv. Funct. Mater. 31 (2021) 2106047 https://doi.org/10.1002/adfm.202106047.
- [52] V. Pamidi, S. Trivedi, S. Behara, M. Fichtner, M.A. Reddy, iScience 25 (2022) 104205 https://doi.org/10.1016/j.isci.2022.104205.

- [53] C. Koo, D. Kwon, S.-J. Park, J. Lee, G.-H. Yoon, S. Hyun Song, T.-Y. Jeon, H. Kang, H. Kim, D. Kim, S.-H. Yu, Chem. Eng. J. 446 (2022) 137429
  <a href="https://doi.org/10.1016/j.cej.2022.137429">https://doi.org/10.1016/j.cej.2022.137429</a>.
- [54] S. Jamil, Y. Feng, M. Fasehullah, G. Ali, B. Wu, Y.-J. Guo, B. Jabar, A. Mansoor, Y.-B. Niu, M. Xu, Chem. Eng. J. 471 (2023) 144450 <a href="https://doi.org/10.1016/j.cej.2023.144450">https://doi.org/10.1016/j.cej.2023.144450</a>.
- [55] L. Zhang, J. Wang, J. Li, G. Schuck, M. Winter, G. Schumacher, J. Li, Nano Energy 70 (2020) 104535 https://doi.org/10.1016/j.nanoen.2020.104535.
- [56] Z. Cheng, B. Zhao, Y.-J. Guo, L. Yu, B. Yuan, W. Hua, Y.-X. Yin, S. Xu, B. Xiao, X. Han, P.-F. Wang, Y.-G. Guo, Adv. Energy Mater. 12 (2022) 2103461 <a href="https://doi.org/10.1002/aenm.202103461">https://doi.org/10.1002/aenm.202103461</a>.
- [57] W. Kang, D.Y.W. Yu, P.-K. Lee, Z. Zhang, H. Bian, W. Li, T.-W. Ng, W. Zhang, C.-S. Lee, ACS Appl. Mater. Interfaces 8 (2016) 31661-31668 <a href="https://doi.org/10.1021/acsami.6b10841">https://doi.org/10.1021/acsami.6b10841</a>.
- [58] J.F. Moulder, J. Chastain, Handbook of X-ray Photoelectron Spectroscopy: A Reference Book of Standard Spectra for Identification and Interpretation of XPS Data, Physical Electronics Division, Perkin-Elmer Corporation1992.
- [59] S. Hüfner, Photoelectron spectroscopy: principles and applications, Springer Science & Business Media2013.
- [60] A. Eftekhari, Sustain. Energy Fuels . 1 (2017) 2053-2060 http://dx.doi.org/10.1039/C7SE00350A.
- [61] X. Li, X. Shen, J. Zhao, Y. Yang, Q. Zhang, F. Ding, M. Han, C. Xu, C. Yang, H. Liu, Y.-S. Hu, ACS Appl. Mater. Interfaces 13 (2021) 33015-33023 https://doi.org/10.1021/acsami.1c07554.

- [62] Y.-N. Zhou, Z. Xiao, D. Han, S. Wang, J. Chen, W. Tang, M. Yang, L. Shao, C. Shu, W. Hua, D. Zhou, Y. Wu, J. Mater. Chem. A 11 (2023) 2618-2626 <a href="https://doi.org/10.1039/D2TA09277H">https://doi.org/10.1039/D2TA09277H</a>.
- [63] L. Tan, Q. Wu, Z. Liu, Q. Chen, H. Yi, Z. Zhao, L. Song, S. Zhong, X. Wu, L. Li, J. Colloid Interface Sci. 622 (2022) 1037-1044 https://doi.org/10.1016/j.jcis.2022.04.112.
- [64] A.J. Toumar, S.P. Ong, W.D. Richards, S. Dacek, G. Ceder, Phys. Rev. Appl. 4 (2015) 064002 https://doi.org/10.1103/PhysRevApplied.4.064002.
- [65] J. Zhang, W. Wang, W. Wang, S. Wang, B. Li, ACS Appl. Mater. Interfaces 11 (2019) 22051-22066 <a href="https://doi.org/10.1021/acsami.9b03937">https://doi.org/10.1021/acsami.9b03937</a>.
- [66] A. Kulka, C. Marino, K. Walczak, C. Borca, C. Bolli, P. Novák, C. Villevieille, J. Mater. Chem. A 8 (2020) 6022-6033 http://dx.doi.org/10.1039/C9TA12176E.
- [67] M. Keller, D. Buchholz, S. Passerini, Adv. Energy Mater. 6 (2016) 1501555 https://doi.org/10.1002/aenm.201501555.
- [68] W. Zuo, X. Liu, J. Qiu, D. Zhang, Z. Xiao, J. Xie, F. Ren, J. Wang, Y. Li, G.F. Ortiz, W. Wen, S. Wu, M.-S. Wang, R. Fu, Y. Yang, Nat. Commun. 12 (2021) 4903 https://doi.org/10.1038/s41467-021-25074-9.

## [Supporting Information]

# Identification of Optimal Composition with Superior Electrochemical Properties Along the Zero Mn<sup>3+</sup> Line in Na<sub>0.75</sub>(Mn-Al-Ni)O<sub>2</sub> Pseudo Ternary System

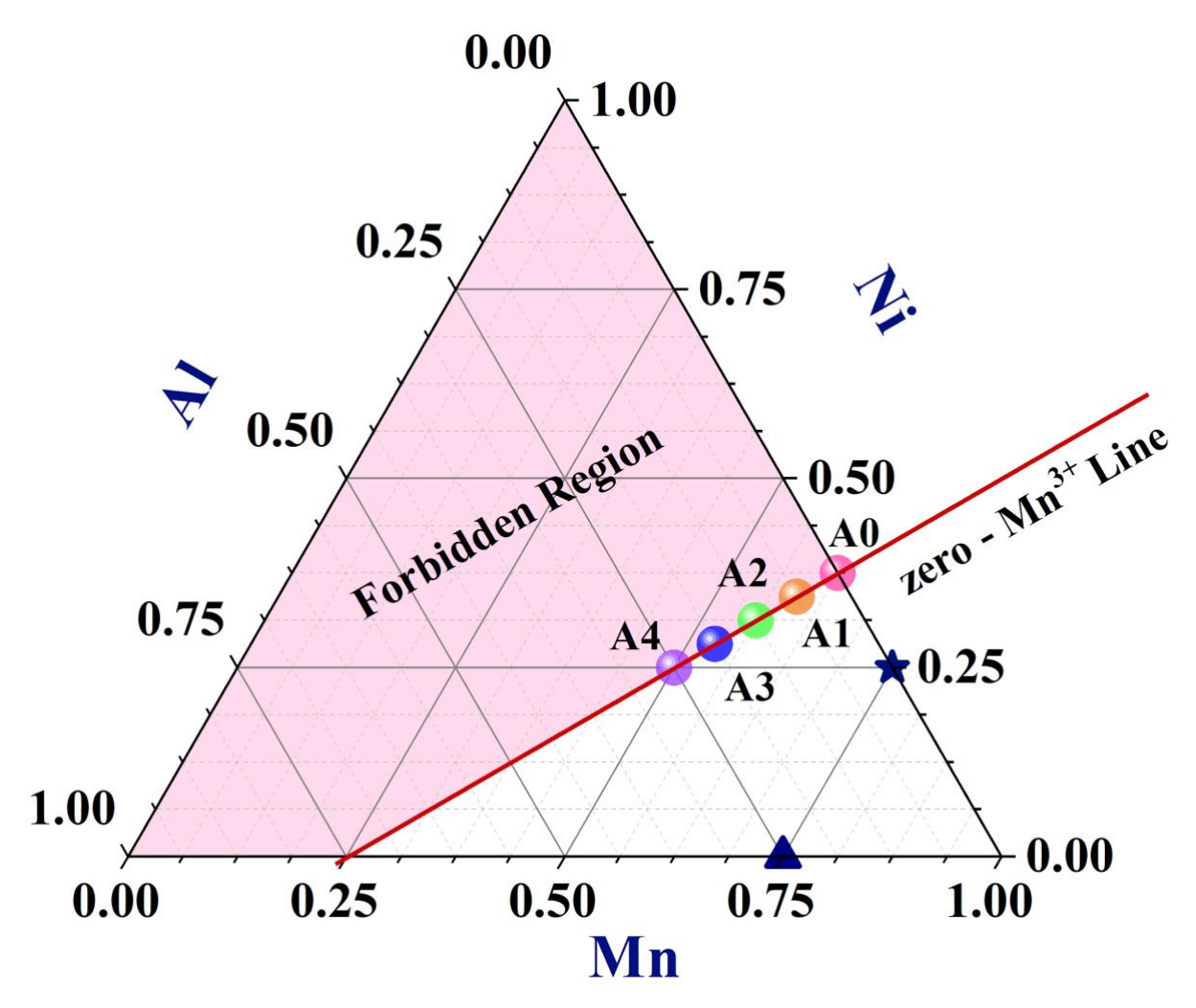


Fig. S1. Pseudo-ternary diagram of the Na<sub>3/4</sub>(Mn-Al-Ni)O<sub>2</sub> system with a star (★) and triangle (▲) symbols representing the compositions studied in References [1] and [2], respectively.

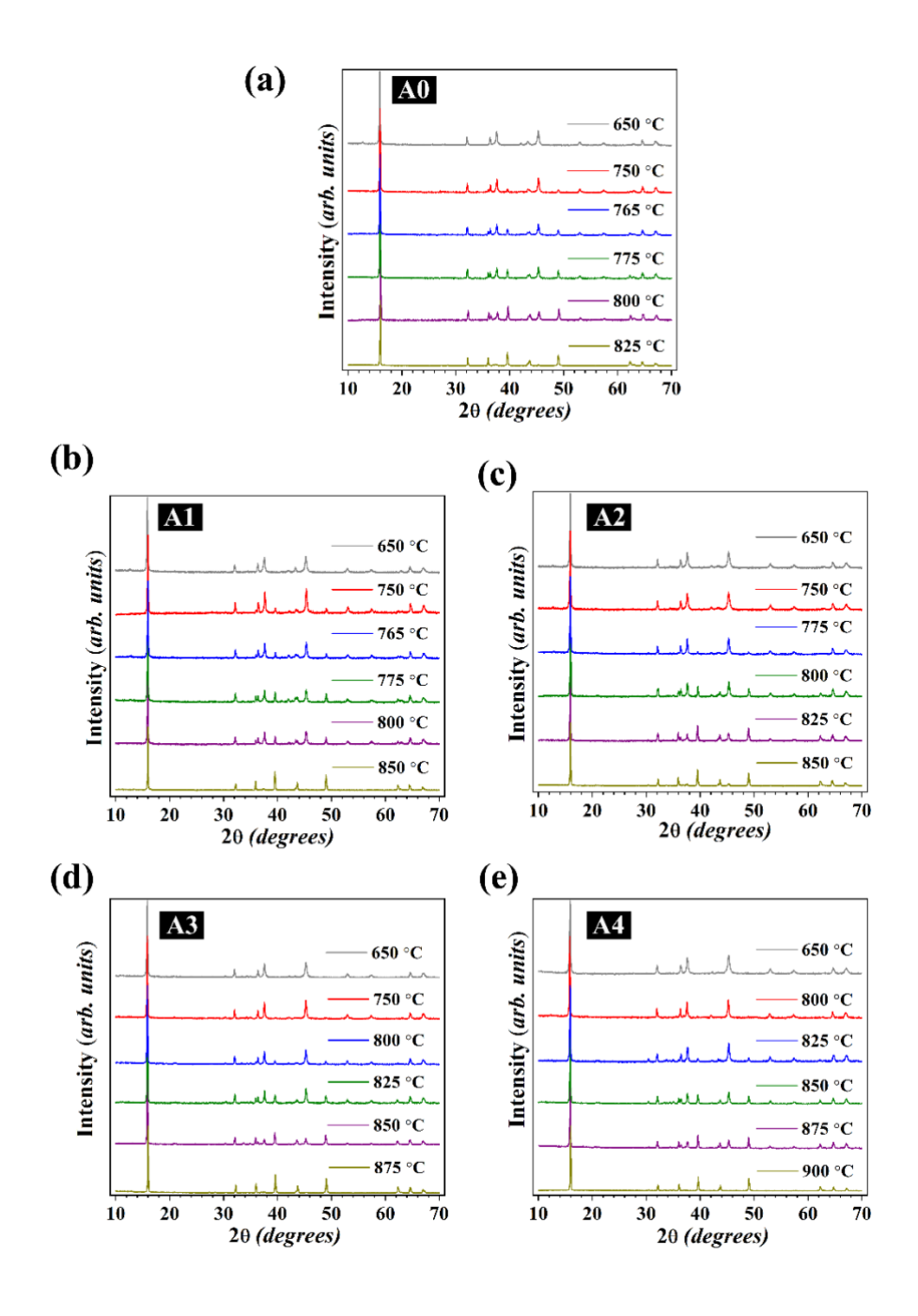


Fig. S2. (a-e) Structural evolution of A0-A4 cathode materials with calcination temperature.

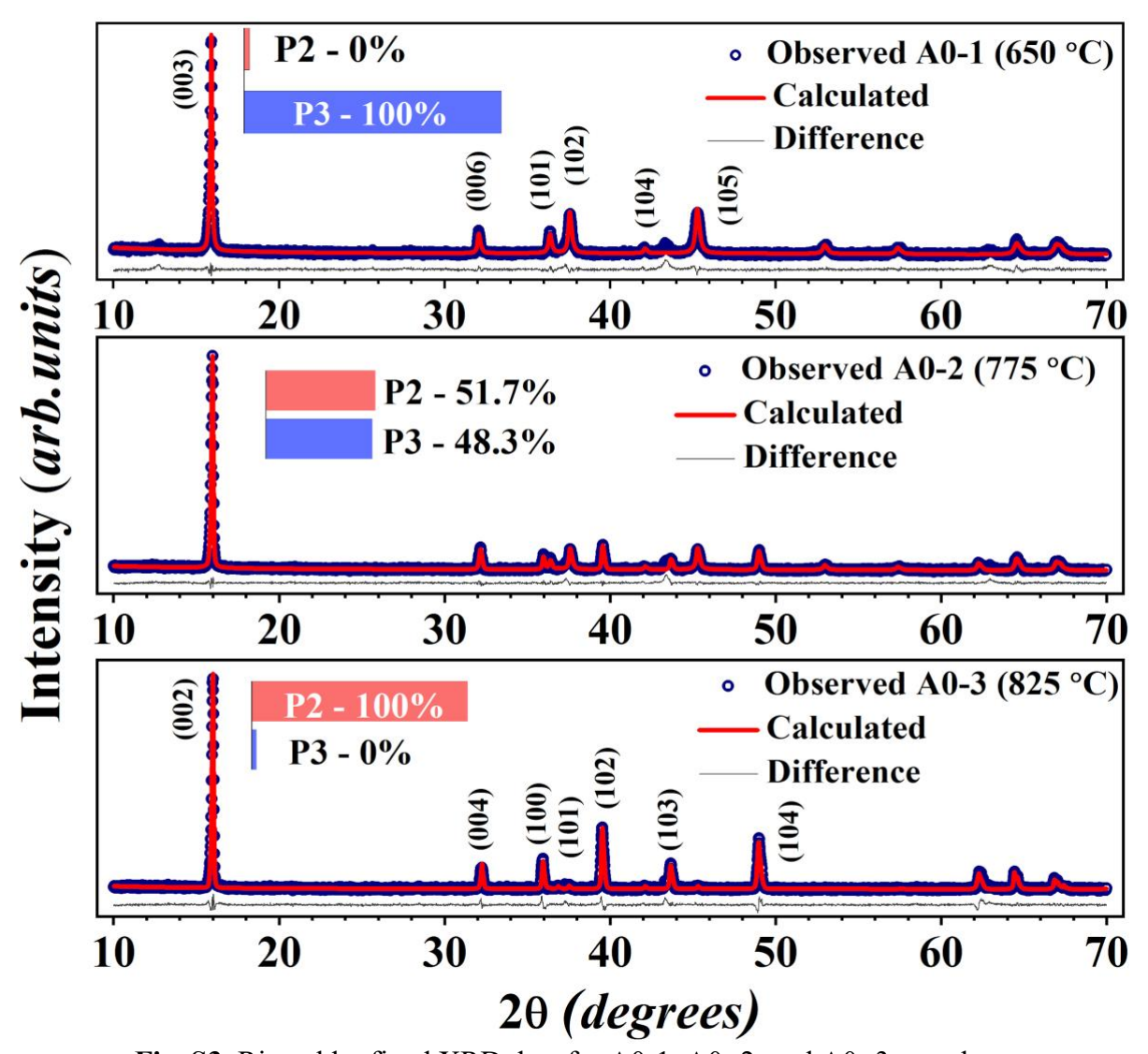


Fig. S3. Rietveld refined XRD data for A0-1, A0-2, and A0-3 samples.

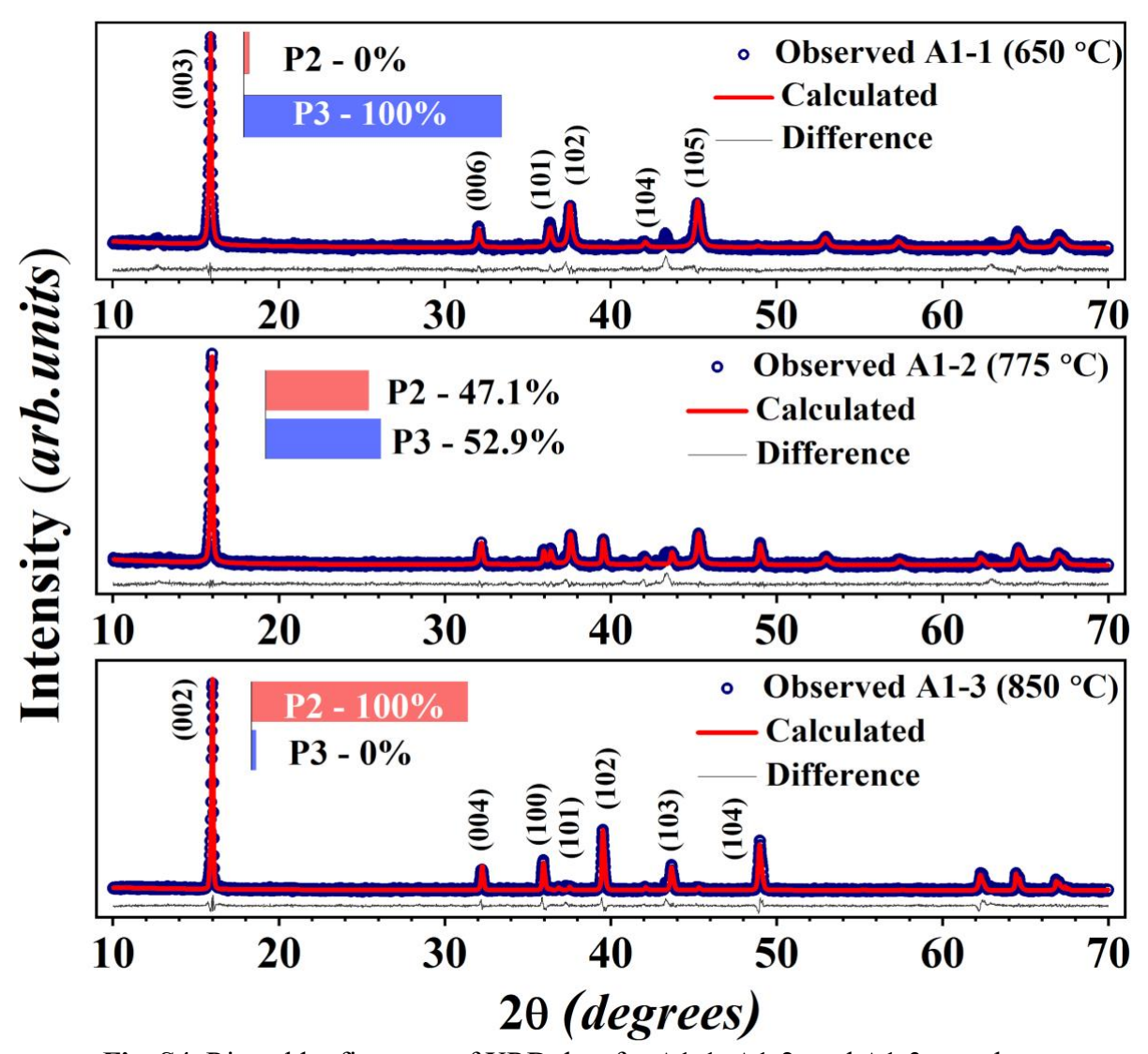


Fig. S4. Rietveld refinement of XRD data for A1-1, A1-2, and A1-3 samples.

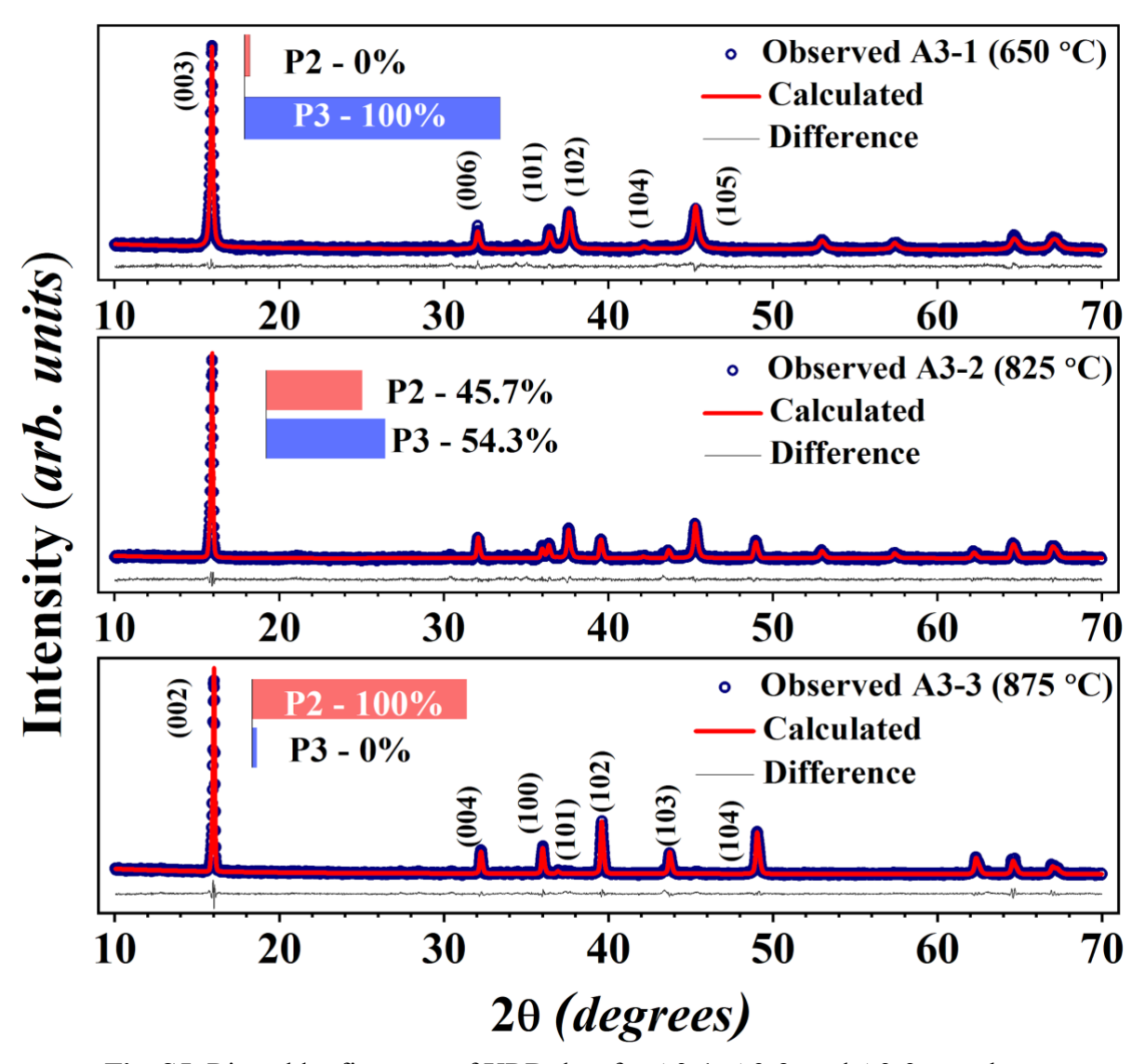


Fig. S5. Rietveld refinement of XRD data for A3-1, A3-2, and A3-3 samples.

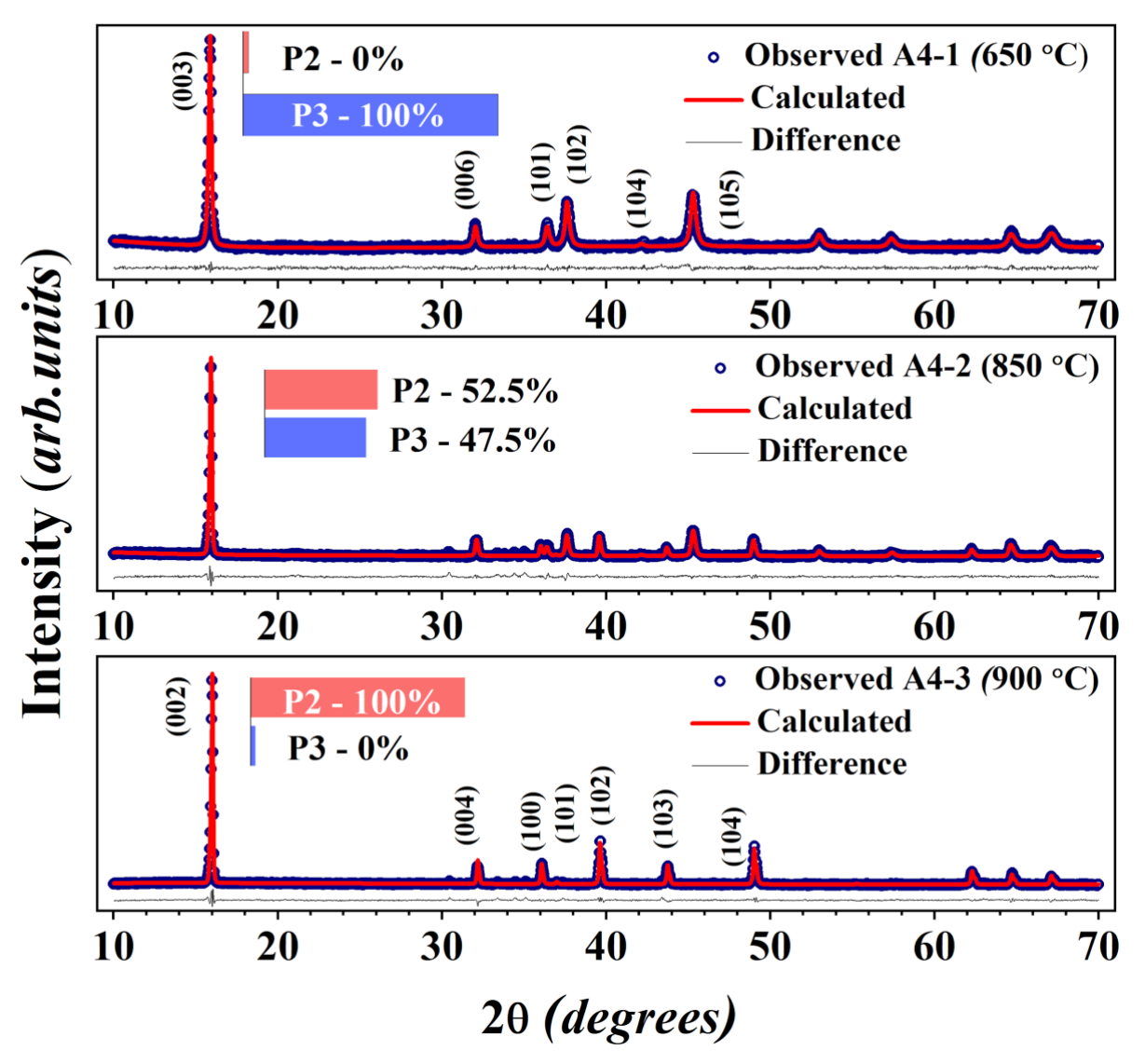
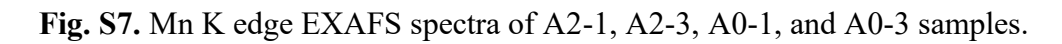
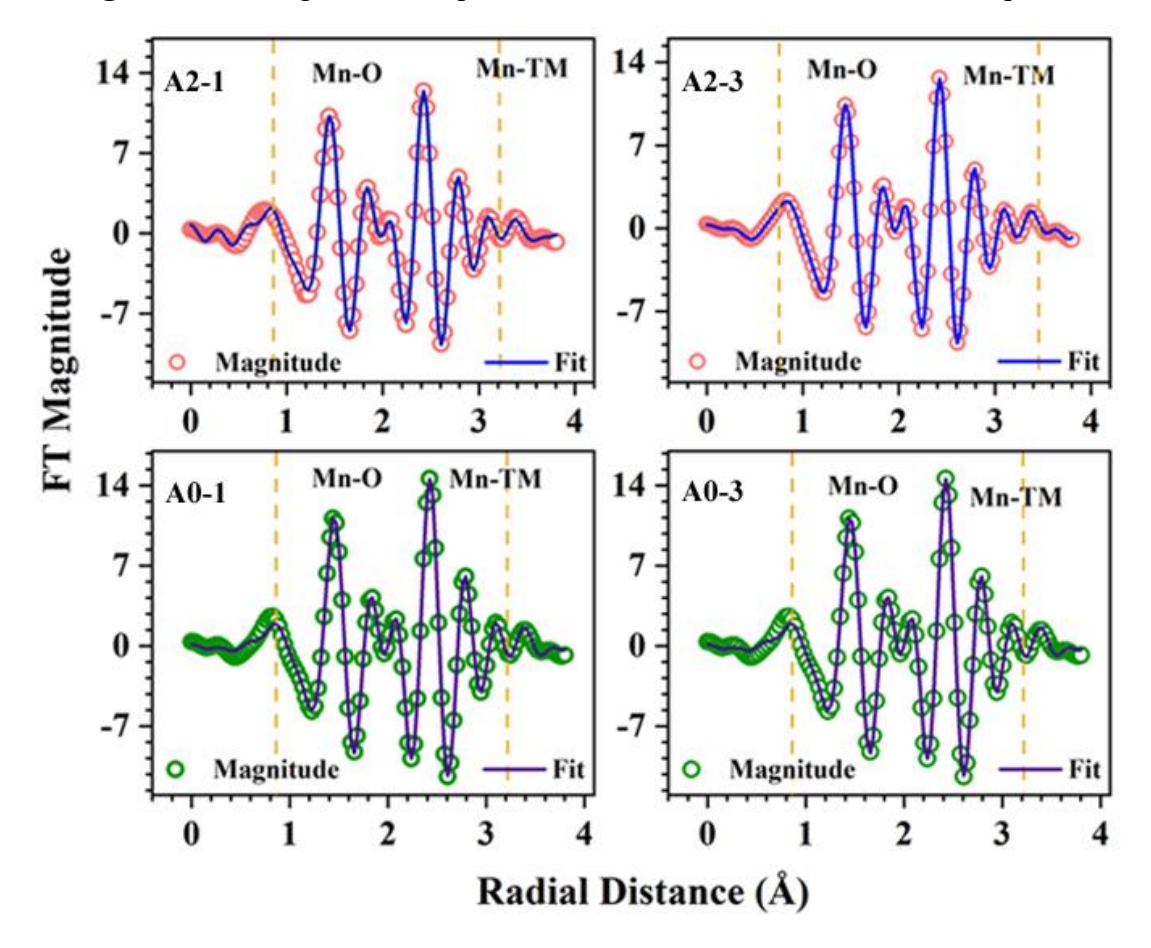
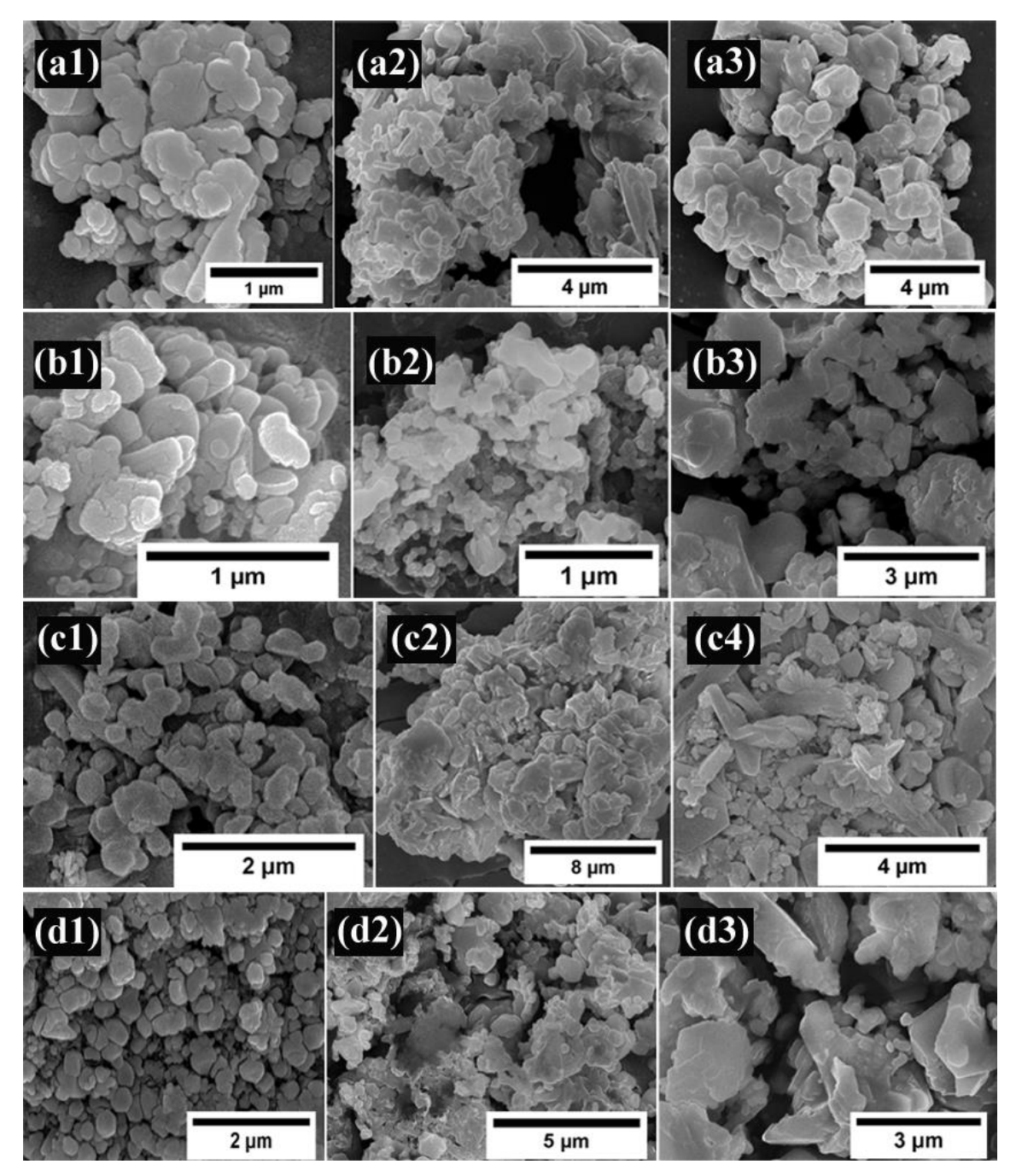


Fig. S6. Rietveld refinement of XRD data for A4-1, A4-2, and A4-3 samples.

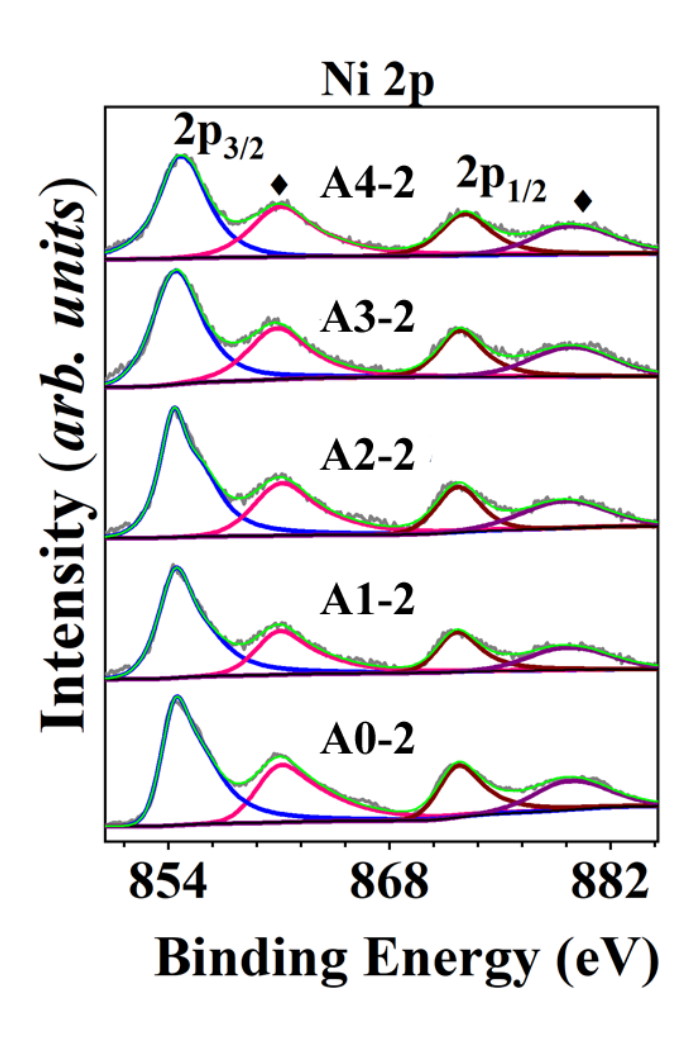


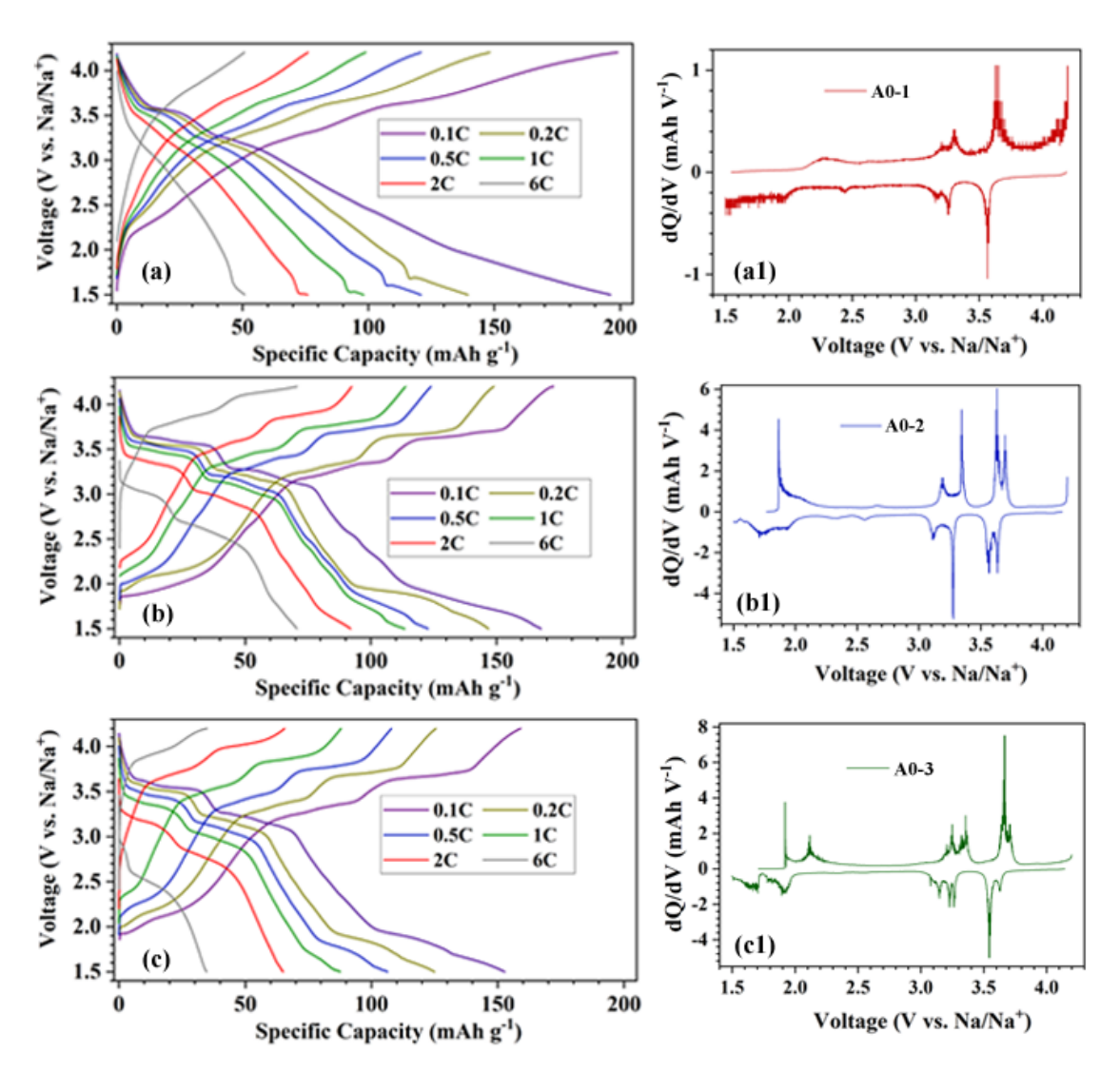




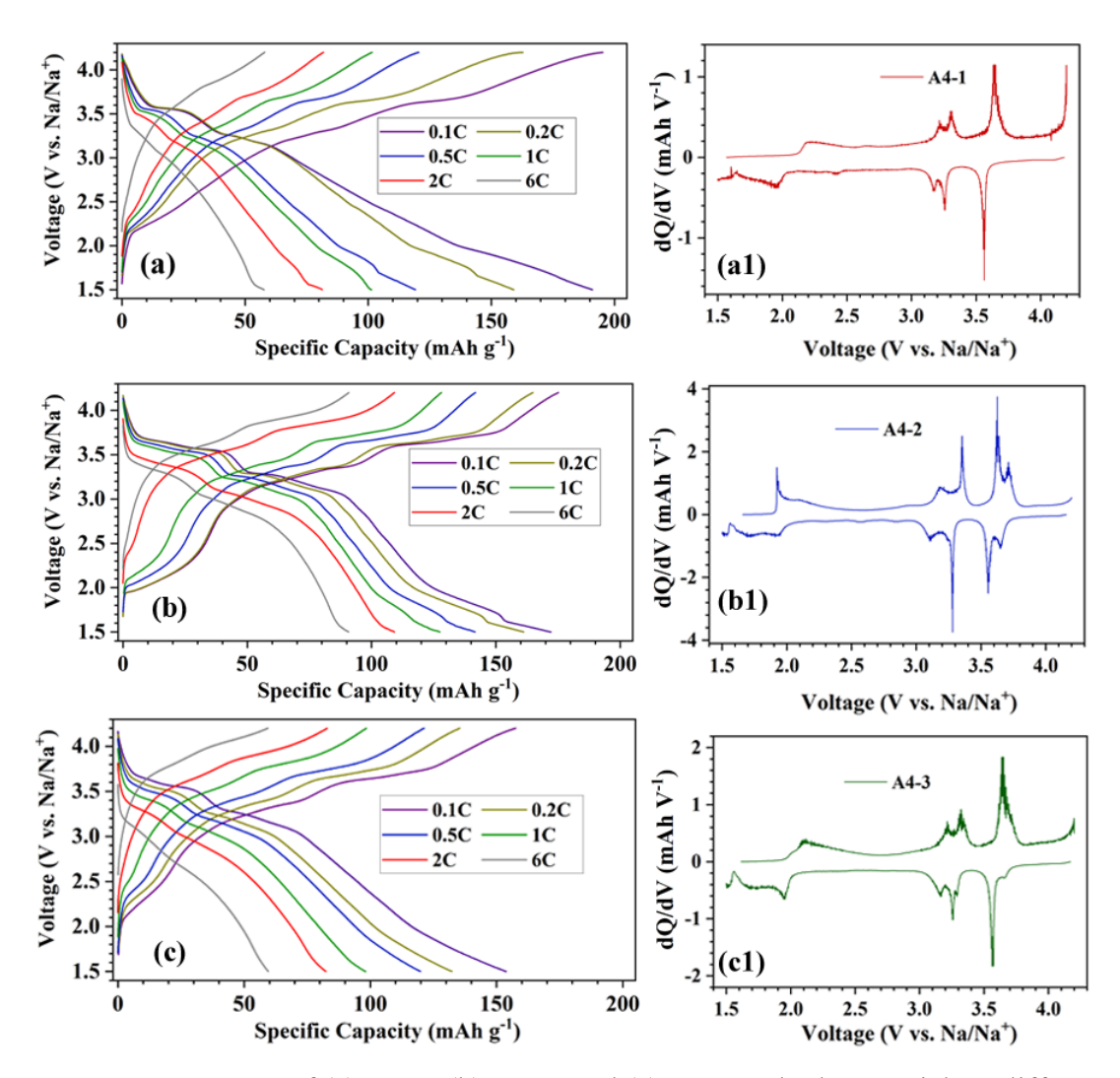
**Fig. S8**. SEM micrographs of (a1) A0-1, (a2) A0-2, (a3) A0-3, (b1) A1-1, (b2) A1-2, (b3) A1-3, (c1) A3-1, (c2) A3-2, (c3) A3-3, (d1) A4-1, (d2) A4-2, and (d3) A4-3 samples.

Fig. S9. Ni 2p XPS plots of A0-2 to A4-2 samples.





**Fig. S10**. GCD curves of (a) A0-1, (b) A0-2, and (c) A0-3 cathode materials at different C rates with (a1-c1) showing their respective dQ/dV vs. voltage (V) plots at 0.1C.



**Fig. S11**. GCD curves of (a) A1-1, (b) A1-2, and (c) A1-3 cathode materials at different C rates with (a1-c1) showing their respective dQ/dV vs. voltage (V) plots at 0.1C.

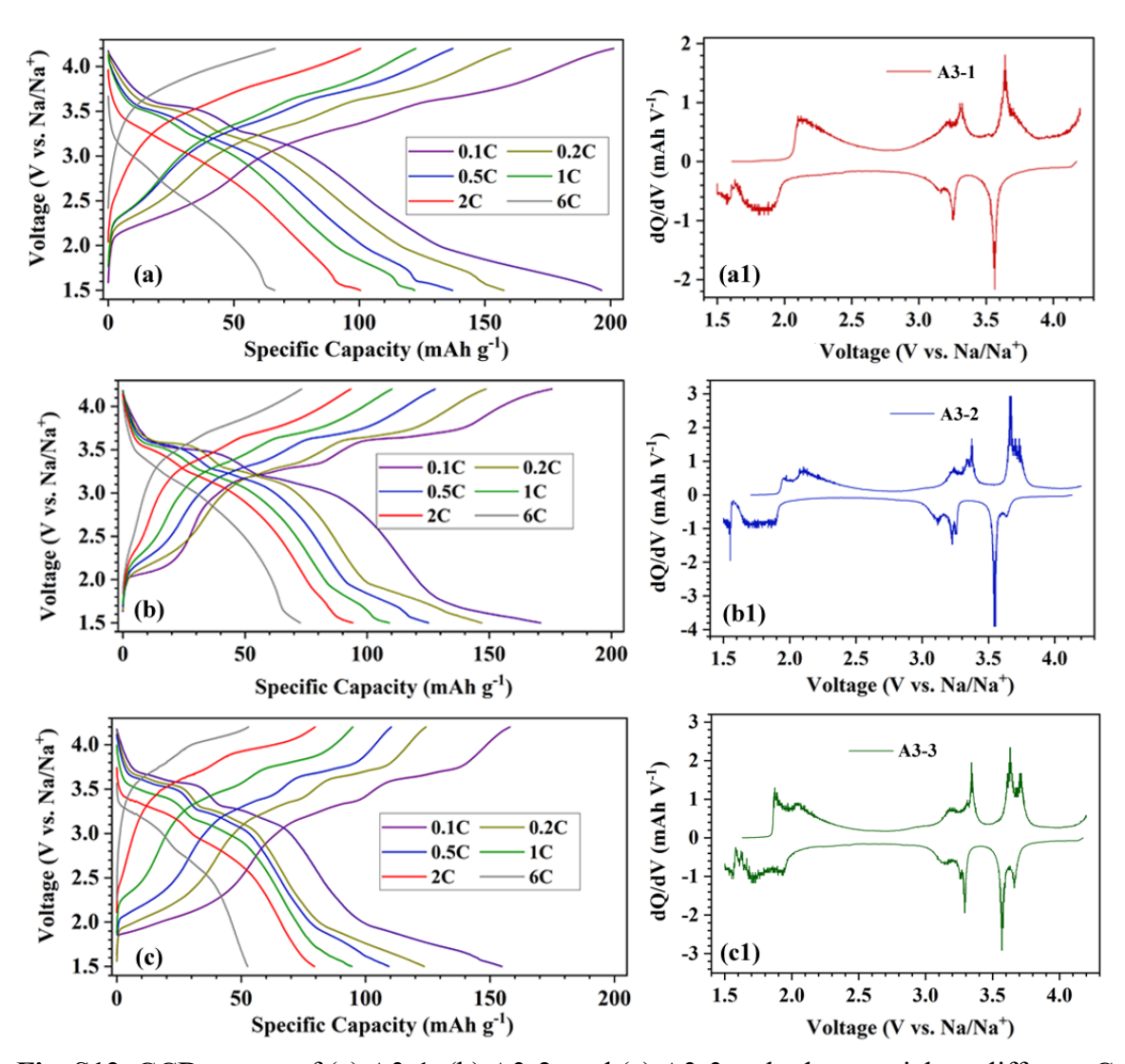


**Fig. S12**. GCD curves of (a) A3-1, (b) A3-2, and (c) A3-3 cathode materials at different C rates with (a1-c1) showing their respective dQ/dV vs. voltage (V) plots at 0.1C.

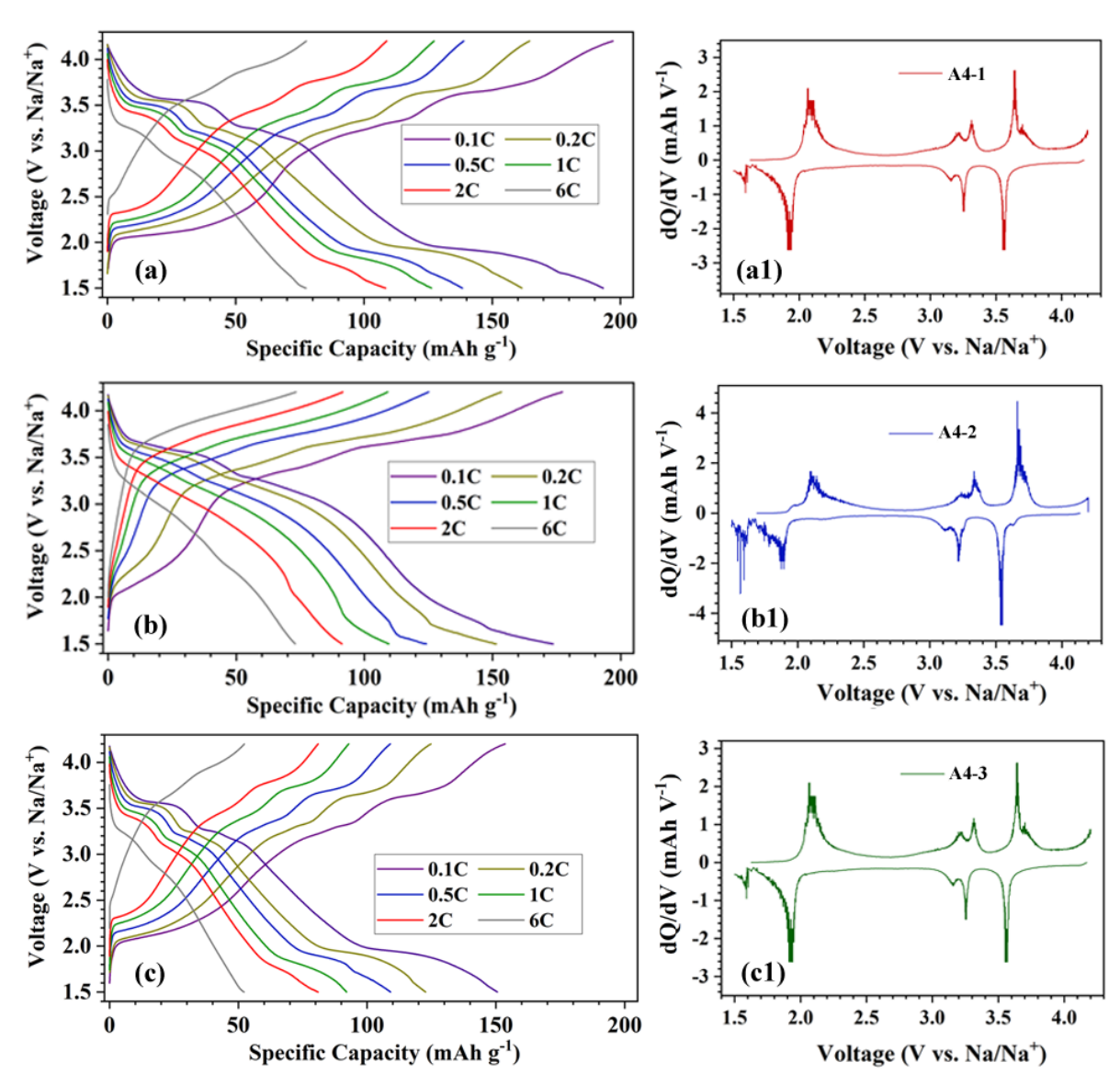


**Fig. S13**. GCD curves of (a) A4-1, (b) A4-2, and (c) A4-3 cathode materials at different C rates with (a1-c1) showing their respective dQ/dV vs. voltage (V) at plots at 0.1C.

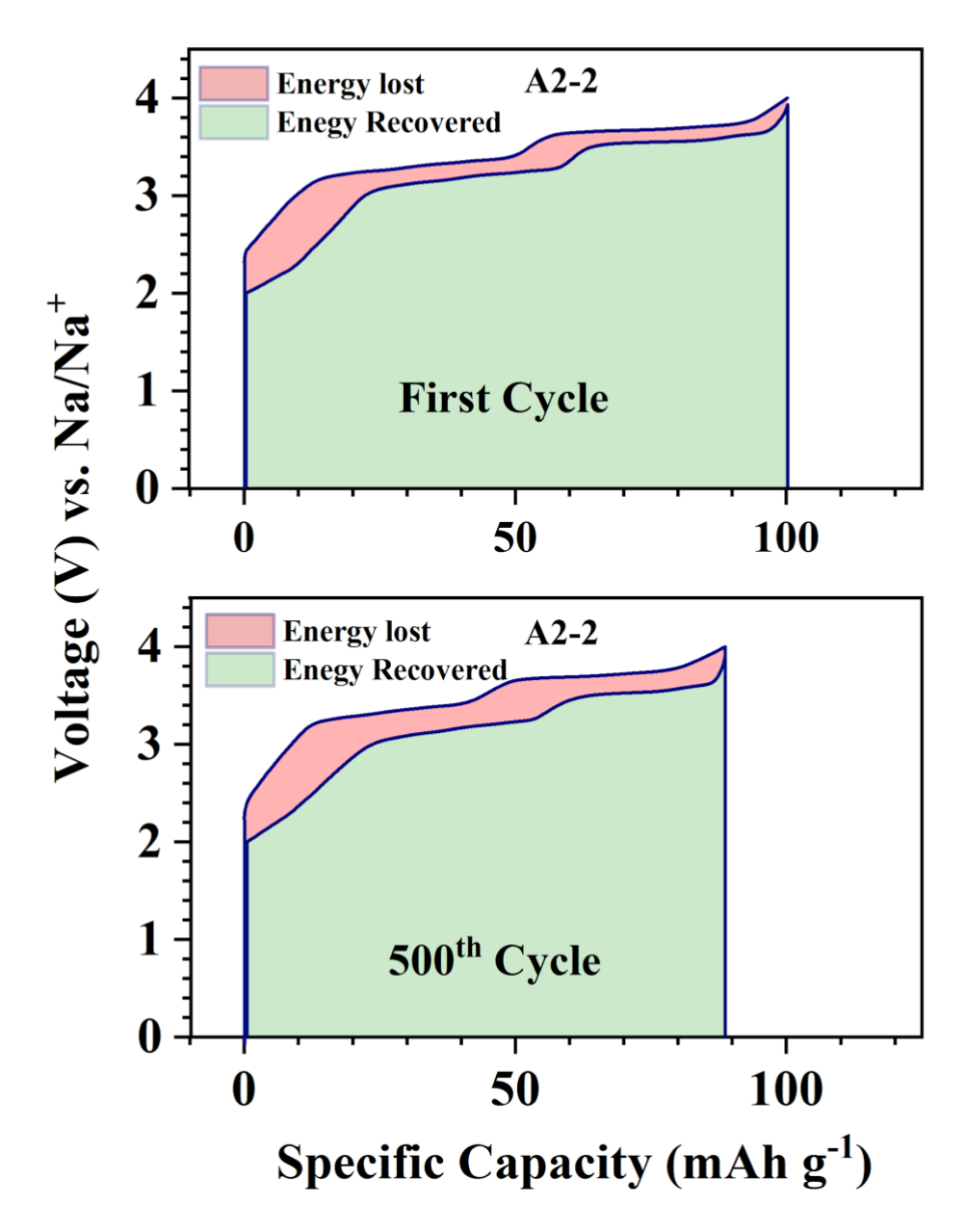


**Fig. S14**. GCD curves of A2-2 depicting energy loss and energy recovered during charge-discharge at 1C.

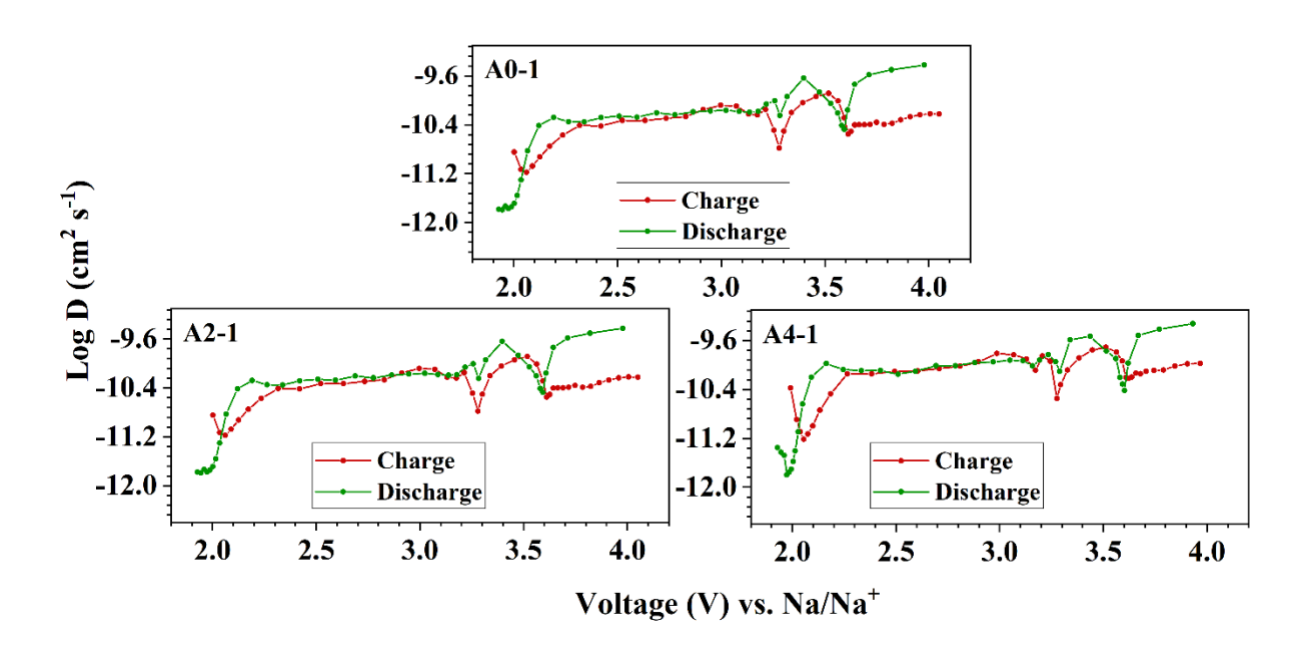


**Fig. S15**. Variation of diffusion coefficients in A0-1, A2-1, and A4-1 cathodes during a charge/discharge cycle.

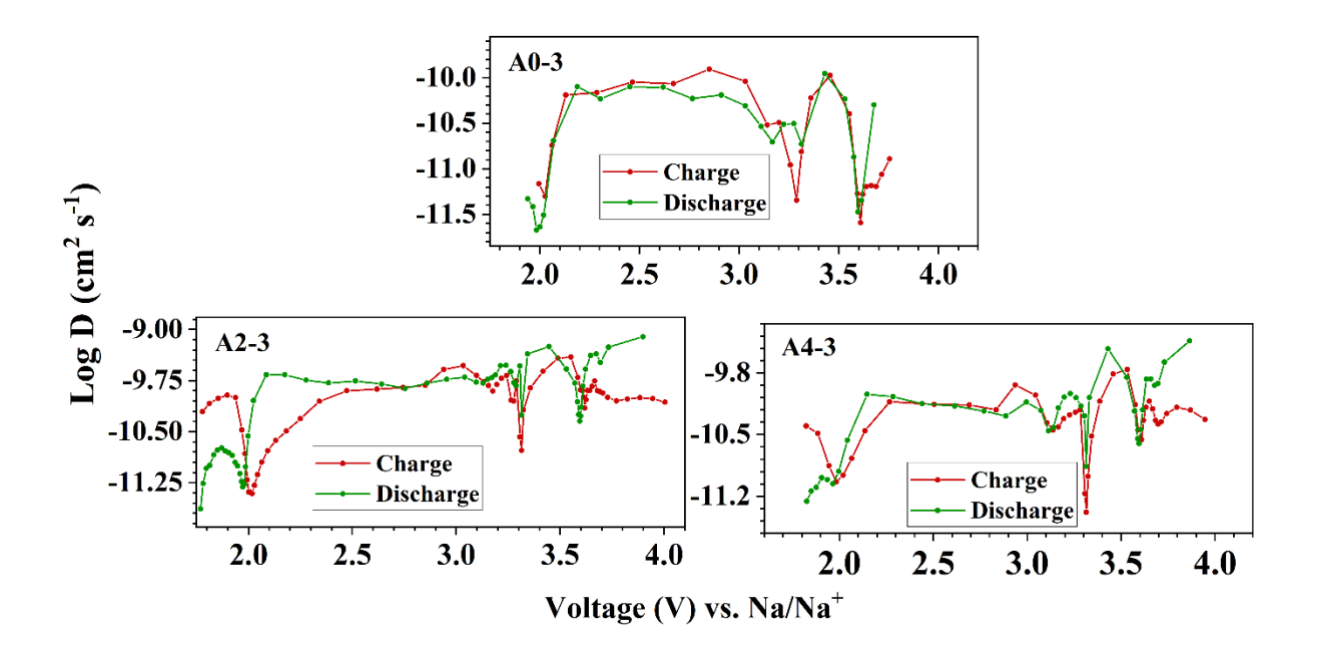


**Fig. S16**. Variation of diffusion coefficients in A0-3, A2-3, and A4-3 cathodes during a charge/discharge cycle.

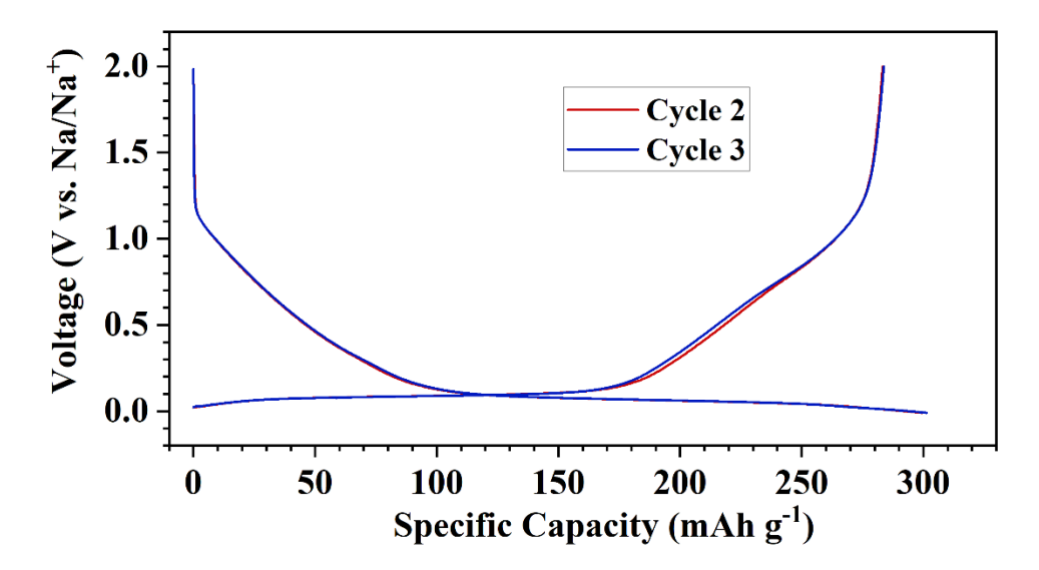


Fig. S17. GCD curves of hard carbon half-cell cycled at 0.05C.

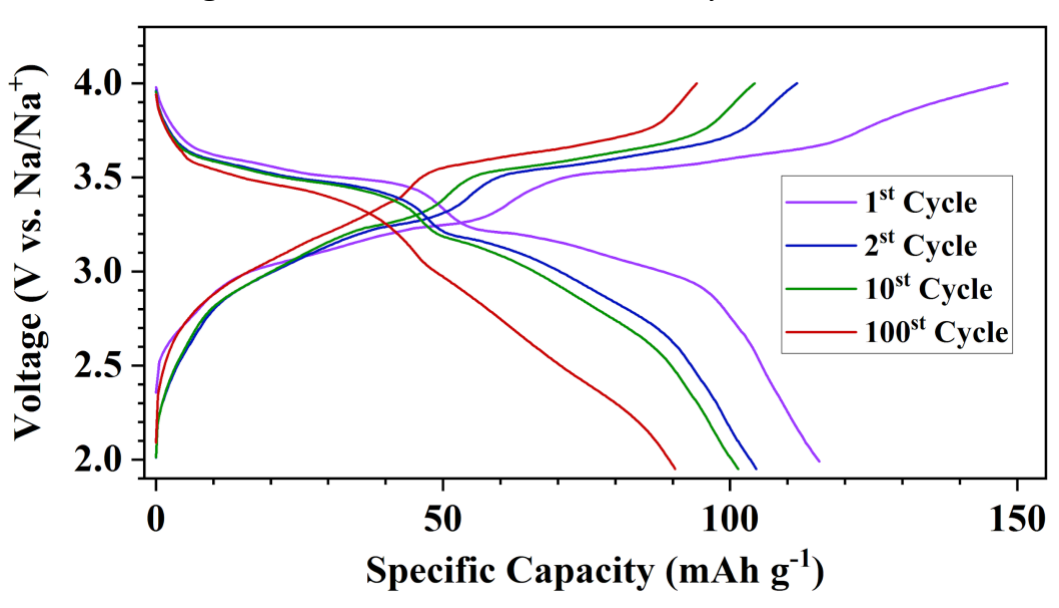


Fig. S18. GCD curves of A2-2 full cells cycled at 0.2C.

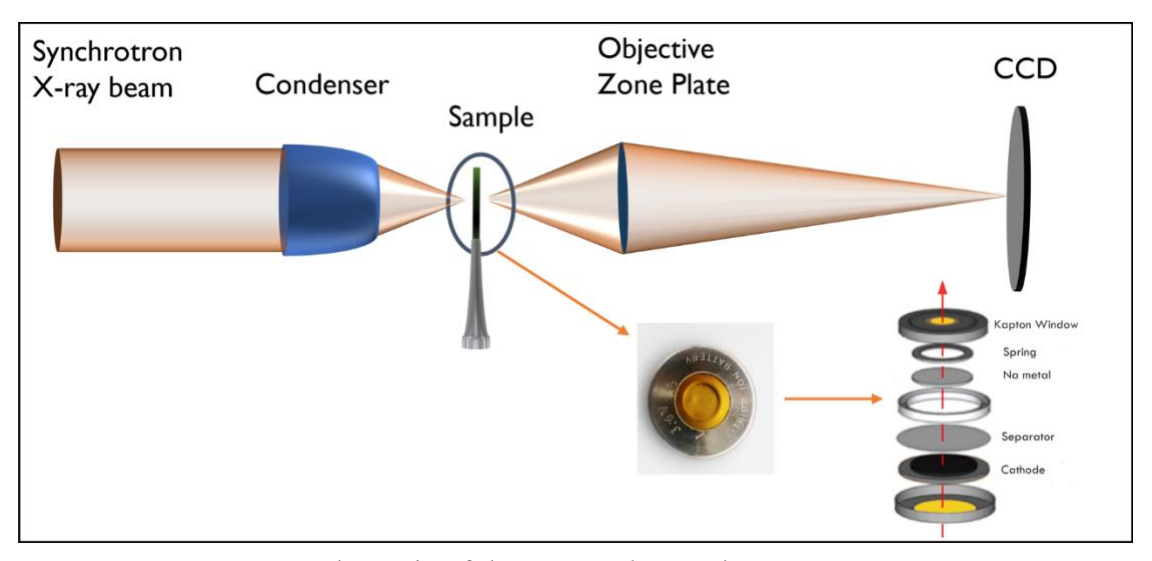
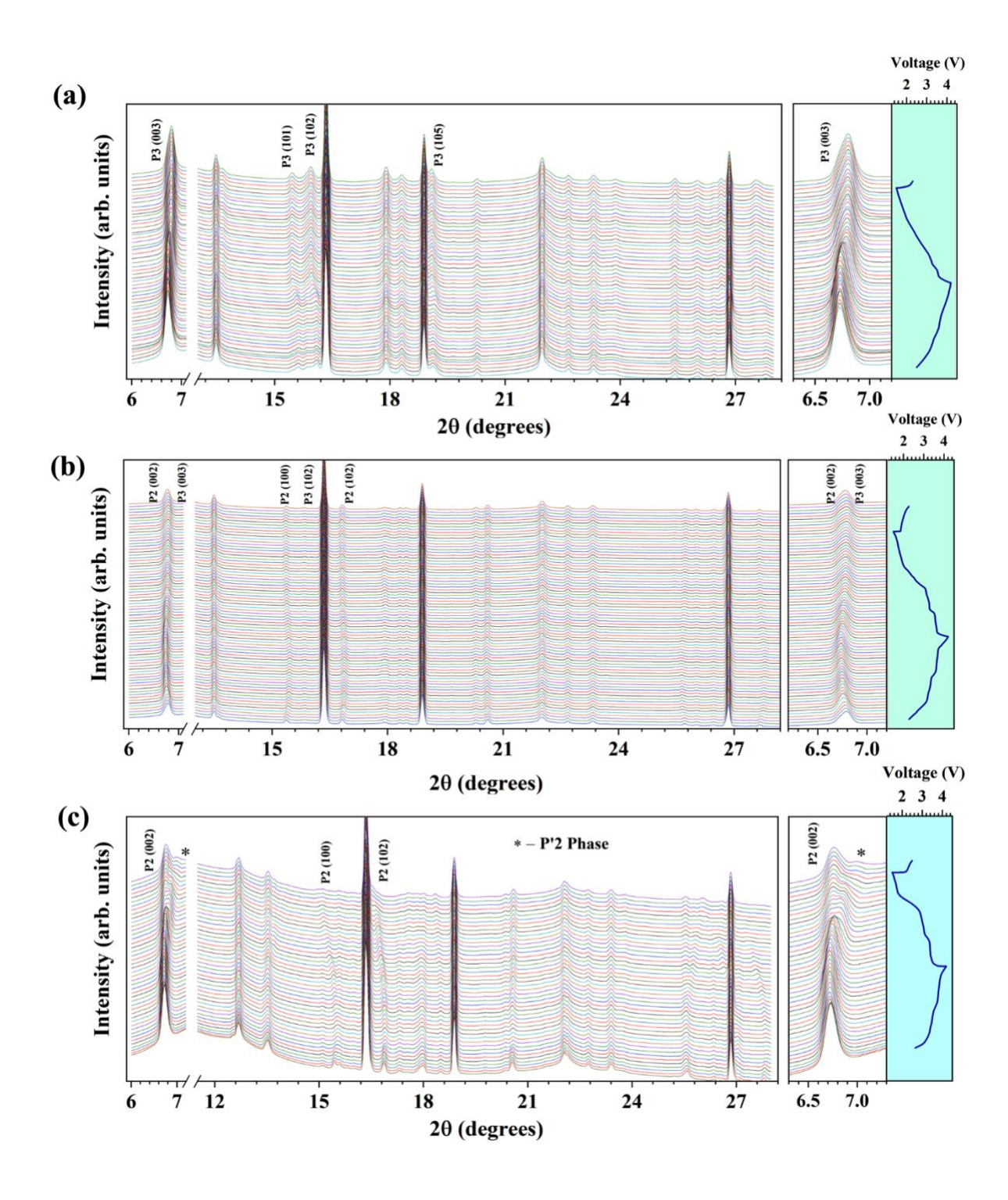
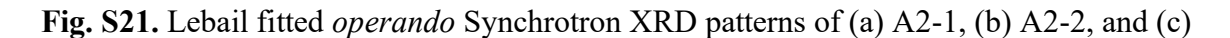
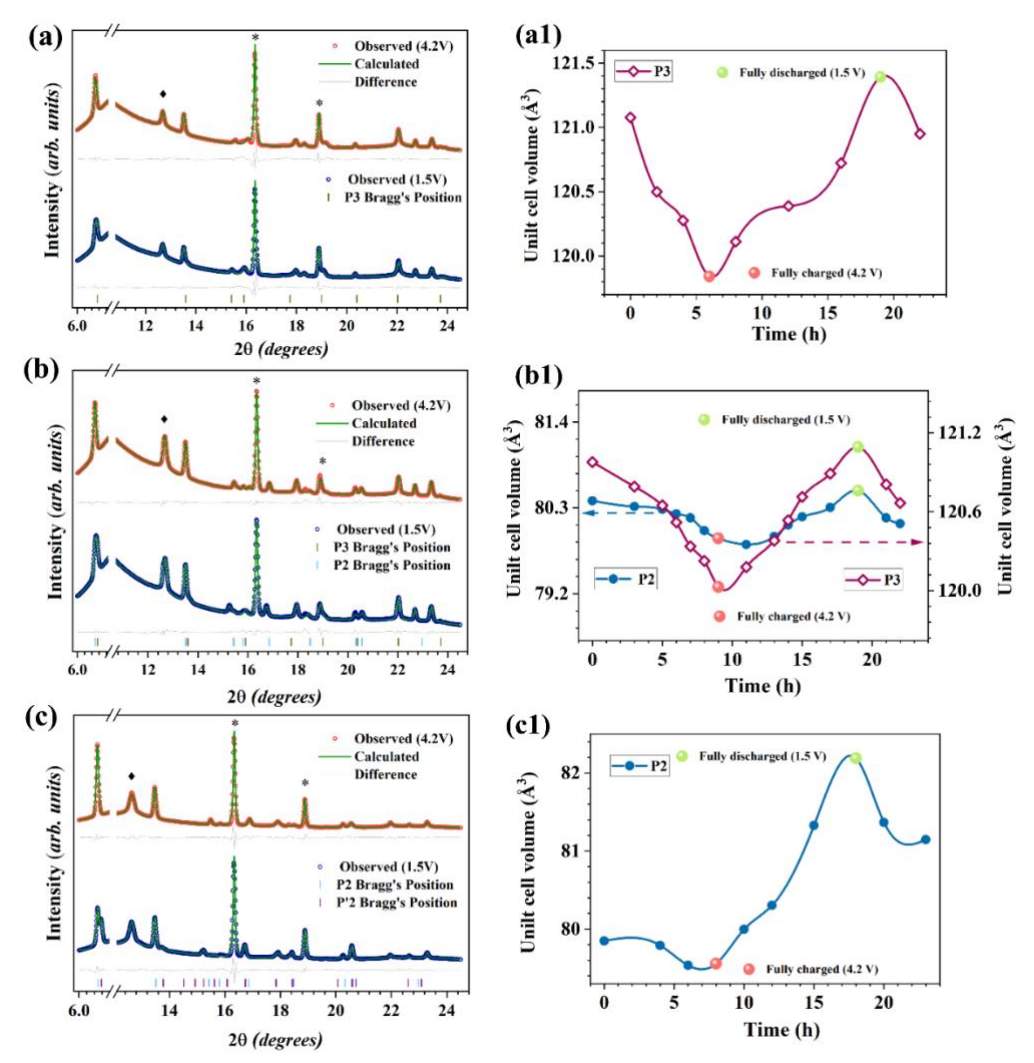


Fig S19. Schematic of the operando Synchrotron XRD setup



**Fig. S20**. *Operando* synchrotron XRD patterns of half-cells employing (a) A4-1, (b) A4-2, and (c) A4-3 samples as cathodes collected during the first charge/discharge cycle.





A2-3 cathodes obtained at fully charged (4.2 V) and fully discharged (1.5 V) states with (a1-c1) depicting their respective variations in P2 and P3 unit cell volumes during cycling.

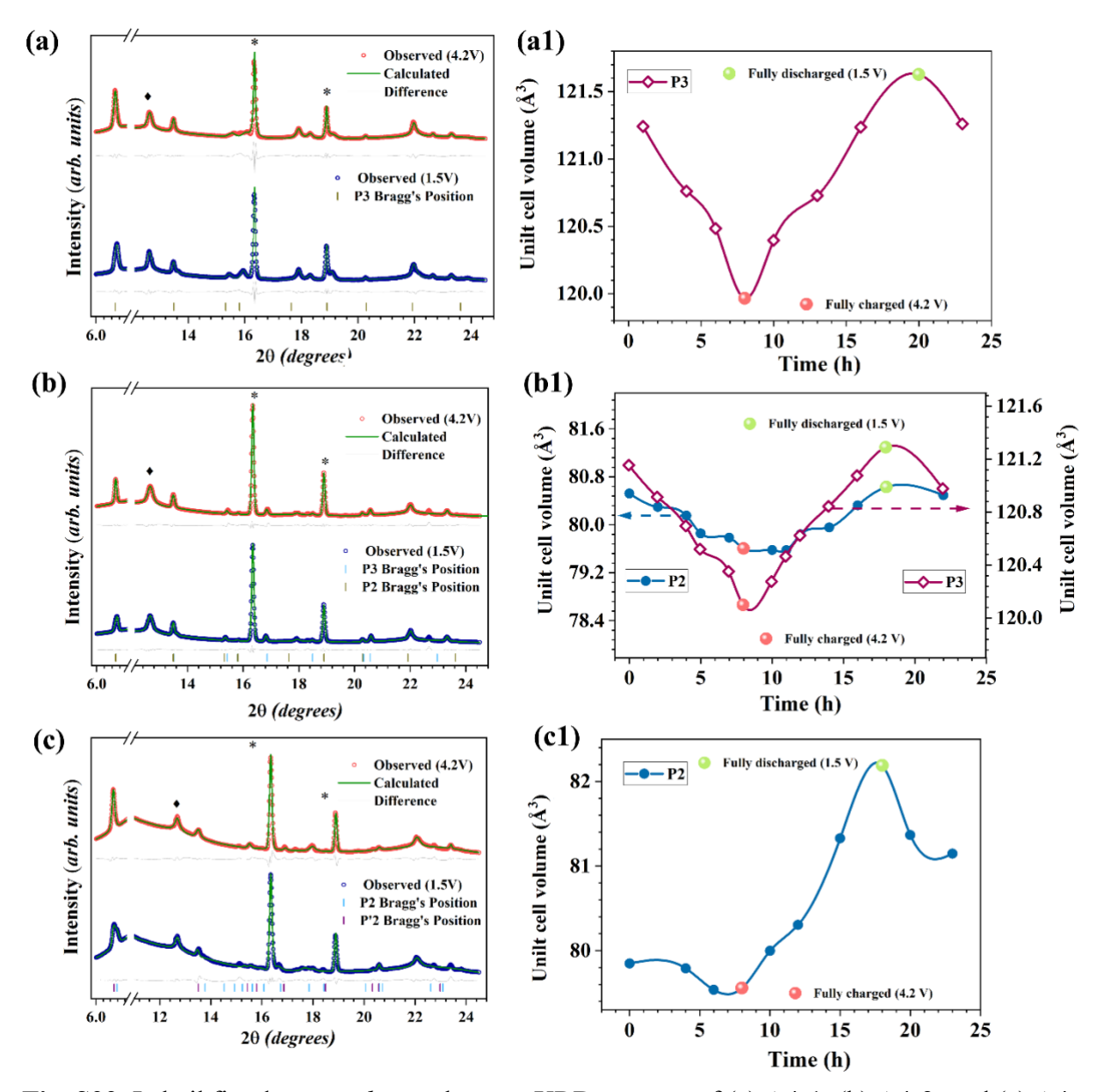


**Fig. S22**. Lebail fitted *operando* synchrotron XRD patterns of (a) A4-1, (b) A4-2, and (c) A4-3 cathodes obtained at fully charged (4.2 V) and fully discharged (1.5 V) states with (a1-c1) depicting their respective variations in unit cell volume of P2 and P3 phases during cycling.

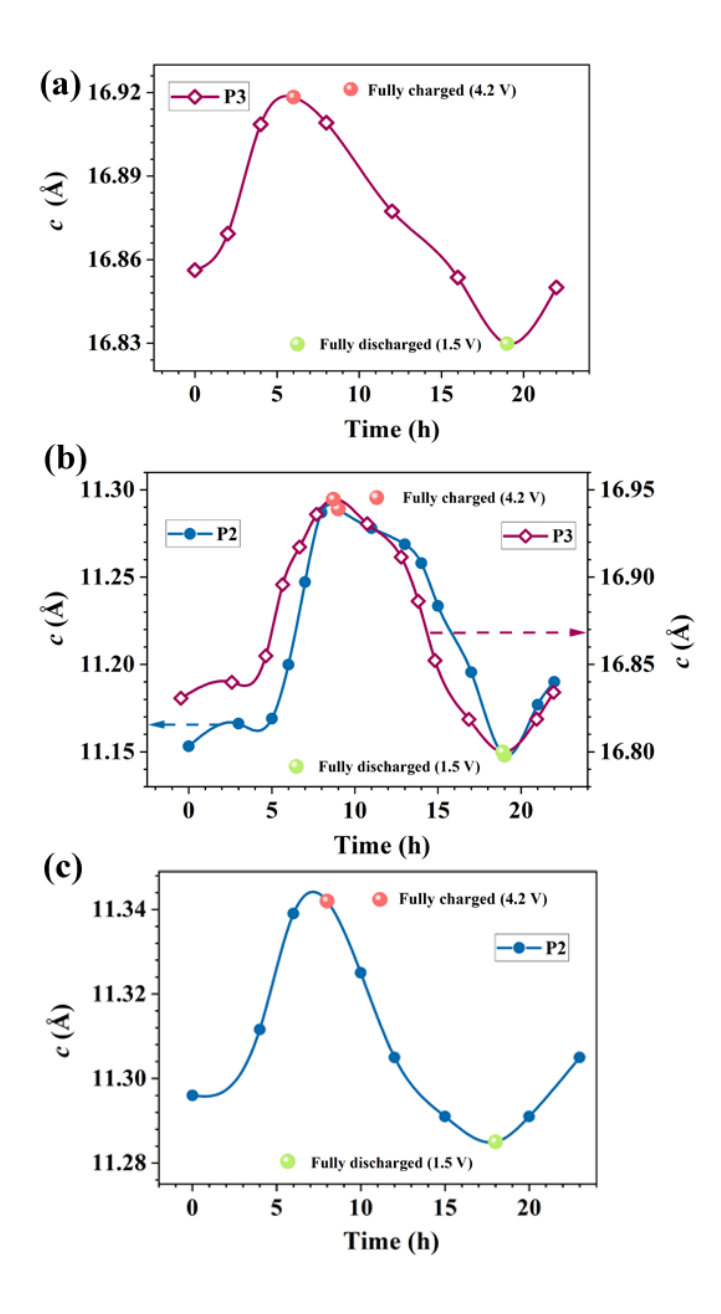


**Fig. S23**. Variation in the *c* parameter of P2 and P3 phases in (a) A2-1, (b) A2-2, and (c) A2-3 cathodes during cycling.

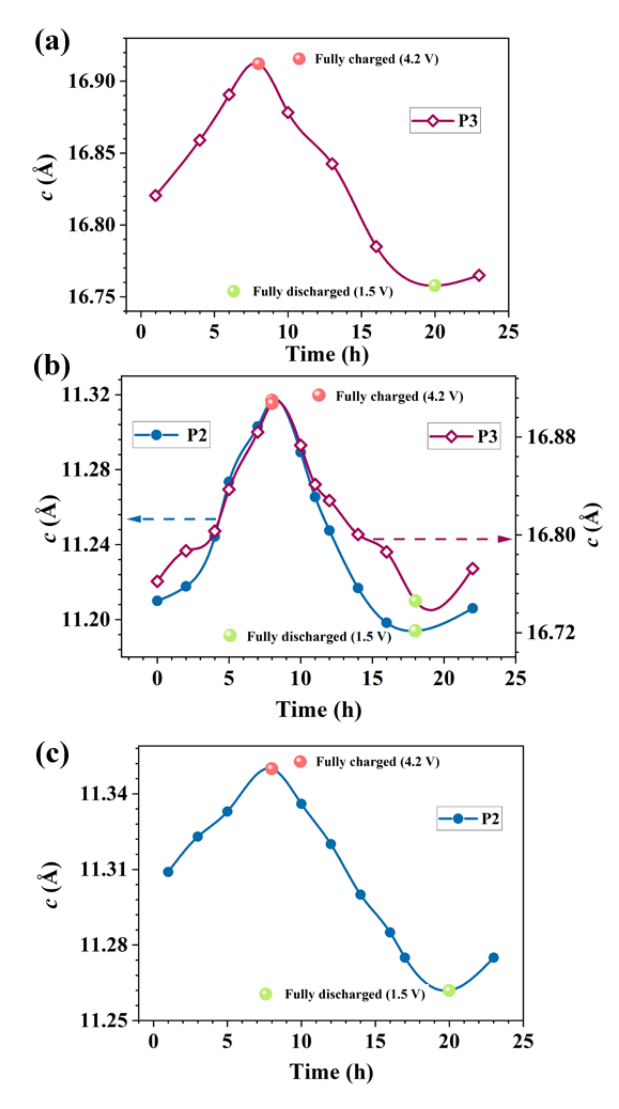


**Fig. S24.** Variation in the *c* parameter of P2 and P3 phases in (a) A4-1, (b) A4-2, and (c)A4-3 cathodes during cycling.

**Table S1.** Lattice parameters of A0 samples obtained from the Rietveld refinement of room temperature XRD data.

Sample	Phase	a (Å)	c (Å)	$V(\mathring{ m A}^3)$	Reliability
	(Fraction)				Factors
					Rexp: 2.92
A0-1	D2 (1000/)	2.8875	16.765	120.92	R <sub>wp</sub> : 4.72
AU-1	P3 (100%)	±0.0001	± 0.001	± 0.01	R <sub>p</sub> : 3.34
					GOF: 1.61
	P3 (48.3%)	2.8879	16.774	121.15	Rexp: 2.89
A0-2		± 0.0002	± 0.002	± 0.02	Rwp: 4.41
110 2	D2 (51 70/)	2.8885	11.15	80.57	$R_p$ : 3.06
	P2 (51.7%)	± 0.0001	± 0.002	± 0.01	GOF: 1.52
					Rexp: 2.99
A0-3	D2(1000/)	2.8885	11.1457	80.53	Rwp: 4.70
	P2(100%)	± 0.0001	± 0.0005	$\pm 0.01$	R <sub>p</sub> : 3.79
					GOF: 1.57

**Table S2.** Lattice parameters of A1 samples obtained from the Rietveld refinement of room temperature XRD data.

Sample	Phase	a (Å)	c (Å)	$V(\mathring{\mathrm{A}}^3)$	Reliability
	(Fraction)				Factors
					Rexp: 2.71
A1-1	D2 (1000/)	2.8885	16.7745	121.21	Rwp: 4.02
A1-1	P3 (100%)	±0.0001	± 0.001	± 0.01	R <sub>p</sub> : 2.86
					GOF: 1.47
	P3 (52.9%)	2.8874	16.757	120.99	Rexp: 3.04
A1-2		± 0.0002	± 0.002	± 0.02	Rwp: 4.51
AI-2	D2 (47 10/)	2.8874	11.134	80.391	$R_p$ : 3.17
	P2 (47.1%)	± 0.0001	± 0.002	± 0.01	GOF: 1.48
					Rexp: 2.69
A1-3	D2(1000/)	2.8878	11.143	80.47	Rwp: 4.31
	P2(100%)	± 0.0001	± 0.001	± 0.01	R <sub>p</sub> : 3.05
					GOF: 1.59

**Table S3.** Lattice parameters of A2 samples obtained from the Rietveld refinement of room temperature XRD data.

Sample	Phase	a (Å)	c (Å)	V (Å <sup>3</sup> )	Reliability
	(Fraction)				Factors
					Rexp: 2.72
A2-1	P3 (100%)	2.8864	16.758	120.92	Rwp: 3.54
A2-1	13 (10070)	±0.0001	± 0.001	± 0.01	R <sub>p</sub> : 2.75
					GOF: 1.3
	P3 (52.6%)	2.8858	16.781	121.04	Rexp: 2.82
A2-2		$\pm 0.0002$	± 0.002	± 0.02	Rwp: 3.43
712 2	P2 (47.4%)	2.8878	11.143	80.47	$R_p$ : 2.65
		± 0.0001	± 0.002	± 0.01	GOF: 1.36
	P2(97%)				Rexp: 2.76
A2-3		2.8881	11.137	80.45	Rwp: 3.30
		± 0.0001	± 0.001	± 0.01	R <sub>p</sub> : 2.57
					GOF: 1.19

**Table S4.** Lattice parameters of A3 samples obtained from the Rietveld refinement of room temperature XRD data.

Sample	Phase	a (Å)	c (Å)	V (Å <sup>3</sup> )	Reliability
	(Fraction)				Factors
					Rexp: 2.67
A3-1	D2 (1000/)	2.8841	16.779	120.87	Rwp: 3.24
A3-1	P3 (100%)	±0.0001	± 0.001	± 0.01	R <sub>p</sub> : 2.54
					GOF: 1.21
	P3 (54.3%)	2.8863	16.7620	120.93	Rexp: 2.73
A3-2		± 0.0001	± 0.002	± 0.02	Rwp: 3.44
A3-2	D2 (45 50()	2.8854	11.163	80.49	$R_p$ : 2.72
	P2 (45.7%)	± 0.0001	± 0.001	± 0.01	GOF: 1.25
					Rexp: 1.98
A3-3	P2(100%)	2.8834	11.1669	80.404	Rwp: 3.41
	12(10070)	± 0.0002	± 0.0004	± 0.005	R <sub>p</sub> : 2.49
					GOF: 1.71

**Table S5.** Lattice parameters of A4 samples obtained from the Rietveld refinement of room temperature XRD data.

Sample	Phase	a (Å)	c (Å)	V (Å <sup>3</sup> )	Reliability
	(Fraction)		, ,	, ,	Factors
					Rexp: 2.23
A4-1	D2 (1000/)	2.8838	16.7924	120.97	R <sub>wp</sub> : 2.51
A4-1	P3 (100%)	±0.0001	± 0.002	± 0.01	R <sub>p</sub> : 1.99
					GOF: 1.12
	P3 (47.5%)	2.8864	16.773	121.00	Rexp: 2.29
A4-2	13 (47.370)	± 0.0001	± 0.001	± 0.02	Rwp: 3.41
A4-2	D2 (52 50/)	2.8842	11.164	80.42	$R_p$ : 2.59
	P2 (52.5%)	± 0.0002	± 0.001	± 0.01	<i>GOF</i> : 1.48
					Rexp: 1.98
A4-3	D2(1000/)	2.8834	11.1669	80.404	Rwp: 3.41
	P2(100%)	± 0.0002	± 0.0004	± 0.005	R <sub>p</sub> : 2.49
					GOF: 1.71

**Table S6**. Cyclic performance of Al-substituted Na-based layered oxide cathodes reported in literature.

Material	Cyclic Performance	Reference	
$Na_{\frac{3}{4}}Mn_{\frac{4.5}{8}}Al_{\frac{1}{8}}Ni_{\frac{2.5}{8}}O_{2}$	85% capacity retention after 500 cycles at 1C	This Work	
Na <sub>0.75</sub> Mn <sub>0.75</sub> Ni <sub>0.25</sub> O <sub>2</sub>	83% capacity retention after 200 cycles at 1C	Ref[1]	
Na <sub>0.75</sub> Mn <sub>0.75</sub> Al <sub>0.25</sub> O <sub>2</sub>	80% capacity retention after 200 cycles at 1C	Ref [2]	
Na0.67Mn0.9Al0.1O2	80% capacity retention after 100 cycles at 0.5C	Ref [3]	
Na2/3Mn8/3Al1/9O2	82.5% capacity retention after 150 cycles at 0.5C	Ref [4]	

Table S7. Percentage changes in unit cell volume of A2 and A4 series of cathodes.

Sample		Maximum percentage change in unit cell volume		
	A4-1	-	1.50%	
<b>A4</b>	A4-2	1.3%	1.0%	
	A4-3	3.6%	-	
	A2-1	-	1.3%	
<b>A2</b>	A2-2	0.8%	0.9%	
	A2-3	3.3%	-	

**Table S8.** Electrochemical properties of A0-2 to A4-2 cathodes

Material	Specific capacity at C/10	Rate performance	Cyclic Performance
$Na_{\frac{3}{4}}Mn_{\frac{5}{8}}Ni_{\frac{3}{8}}O_{2}$ (A0-2)	166 mAh g <sup>-1</sup>	112 mAh g <sup>-1</sup> at 1C 70 mAh g <sup>-1</sup> at 6C	51 % capacity retention after 300 cycles at 1C
$Na_{\frac{3}{4}}Mn_{\frac{4.75}{8}}Al_{\frac{0.5}{8}}Ni_{\frac{2.75}{8}}O_{2}$ (A1-2)	173 mAh g <sup>-1</sup>	125 mAh g <sup>-1</sup> at 1C 84 mAh g <sup>-1</sup> at 6C	69 % capacity retention after 200 cycles at 1C
$Na_{\frac{3}{4}}Mn_{\frac{4.5}{8}}Al_{\frac{1}{8}}Ni_{\frac{2.5}{8}}O_{2}$ <b>(A2-2)</b>	175 mAh g <sup>-1</sup>	127 mAh g <sup>-1</sup> at 1C 92 mAh g <sup>-1</sup> at 6C	79% capacity retention after 300 cycles at 1C
$Na_{\frac{3}{4}}Mn_{\frac{4.25}{8}}Al_{\frac{1.5}{8}}Ni_{\frac{2.25}{8}}O_{2}$ (A3-2)	171 mAh g <sup>-1</sup>	122 mAh g <sup>-1</sup> at 1C 72 mAh g <sup>-1</sup> at 6C	73 % capacity retention after 300 cycles at 1C
$Na_{\frac{3}{4}}Mn_{\frac{4}{8}}Al_{\frac{2}{8}}Ni_{\frac{2}{8}}O_{2}$ (A4-2)	173 mAh g <sup>-1</sup>	110 mAh g <sup>-1</sup> at 1C 73 mAh g <sup>-1</sup> at 6C	69 % capacity retention after 300 cycles at 1C

## References

[1] H.N. Vasavan, M. Badole, S. Saxena, V. Srihari, A.K. Das, P. Gami, S. Deswal, P. Kumar, S.

Kumar, Mater. Today Energy., 37 (2023) 101380

https://doi.org/10.1016/j.mtener.2023.101380.

[2] H.N. Vasavan, M. Badole, S. Saxena, V. Srihari, A.K. Das, P. Gami, S. Deswal, P.

Kumar, S. Kumar, J. Energy Storage, 74 (2023) 109428

https://doi.org/10.1016/j.est.2023.109428.

[3] X. Liu, W. Zuo, B. Zheng, Y. Xiang, K. Zhou, Z. Xiao, P. Shan, J. Shi, Q. Li, G. Zhong,

R. Fu, Y. Yang, Angew. Chem. Int. Ed., 58 (2019) 18086-18095

https://doi.org/10.1002/anie.201911698.

[4] W.-L. Pang, X.-H. Zhang, J.-Z. Guo, J.-Y. Li, X. Yan, B.-H. Hou, H.-Y. Guan, X.-L. Wu,

J. Power Sources, 356 (2017) 80-88 <a href="https://doi.org/10.1016/j.jpowsour.2017.04.076">https://doi.org/10.1016/j.jpowsour.2017.04.076</a>.